

STATEMENT

Name: János Papp
Neptun ID: YA318S

ELTE Faculty of Science: Physics MSc

specialization: Research Physicist Specialization

Title of diploma work: Theoretical Study of Stacking Faults in Rhombohedral Graphite

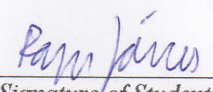
As the author of the diploma work I declare, with disciplinary responsibility that my thesis is my own intellectual product and the result of my own work. Furthermore I declare that I have consistently applied the standard rules of references and citations.

I acknowledge that the following cases are considered plagiarism:

- using a literal quotation without quotation mark and adding citation;
- referencing content without citing the source;
- representing another person's published thoughts as my own thoughts.

Furthermore, I declare that the printed and electronical versions of the submitted diploma work are textually and contextually identical.

Budapest, 2023.05.28.


Signature of Student

Theoretical Study of Stacking Faults in Rhombohedral Graphite

János Papp

Supervisors:

Zoltán Tajkov

Centre for Energy Research, Institute of Technical Physics and Materials Science,

Centre of Low Temperature Physics, Institute of Experimental Physics, Slovak

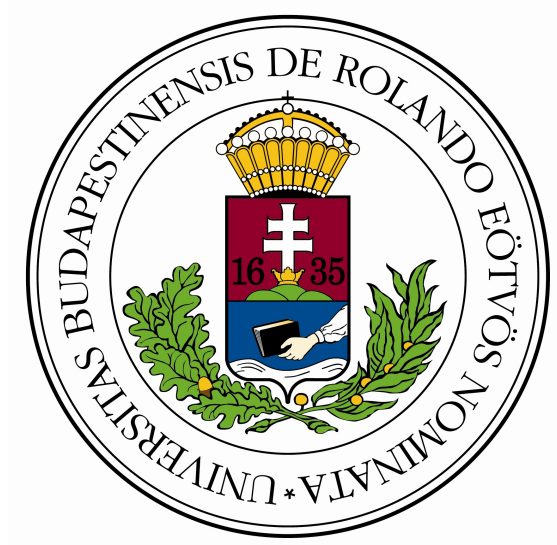
Academy of Sciences, Košice SK-04001, Slovakia

János Koltai

ELTE Faculty of Science Department of Biological Physics

MSc Thesis

2023



Abstract

In this thesis we study the effects of stacking faults in rhombohedral graphite. A low energy tight binding model is used to compute the characteristics of stacking faults and their effect on electrical properties. Utilizing this model the local density of states on the surface can be calculated for the different configurations. Our objective is to aid in the interpretation of data gathered from surface mapping techniques such as scanning tunneling microscopy. To this purpose a machine learning solution is introduced, which can predict the stacking order from the local density of states.

Contents

1	Introduction	5
1.1	The great wide realm of carbon	5
1.2	Structure of the thesis	7
2	Theoretical background	8
2.1	Periodic crystals	8
2.2	Tight binding approximation	9
2.3	Tight binding description of graphene	12
2.4	Density of states	17
2.4.1	Density of states of graphene	17
2.4.2	Projected density of states and numerical calculations	19
2.5	Scanning tunneling microscopy and its connection to LDOS	20
2.5.1	The scanning tunneling microscope	20
2.5.2	Theoretical description of STM	21
3	Rhombohedral graphite and stacking faults	23
3.1	What are the possible stacking configurations?	24
3.2	Tight binding model for stacking faults	26
3.2.1	The Hamiltonian of bilayer graphene	27
3.2.2	Few layer graphene and stacking faults	29
3.3	Comparison of DOS spectra	32
3.3.1	Cross-correlation of functions	32
3.3.2	Decision tree model	33
4	Results	35
4.1	The fault-free systems	35
4.2	The effect of thickness	37
4.3	The effect of a single fault	38
4.4	Transition from ABC to ABA	41
4.5	When do the peaks shine through?	43
4.6	Algorithms to identify sub-structures	44
4.6.1	Cross-correlation function	44
4.7	The performance of the decision tree model	45

CONTENTS

5 Summary and outlook	48
-----------------------	----

1 Introduction

1.1 The great wide realm of carbon

The vast number and variety of the allotropes of carbon has been in the center of attention in solid state physics research for decades now. The different crystalline structures have very different properties and many of them have promising real-world applications [1, 2, 3]. Indeed, many Nobel prizes were awarded to researchers working with carbon. In 1996 the award in Chemistry went to Robert F. Curl, Jr., Sir Harold W. Kroto and Richard E. Smalley for the discovery of fullerenes [4]. It could be argued that all prizes in medicine are carbon-related since all organisms are carbon-based.

Last but no least, I would like to mention Andre Geim and Konstantin Novoselov who got the Nobel Prize in Physics in 2010 for the isolation of graphene [5]. This discovery represented a significant breakthrough in light of the Mermin-Wagner theorem, which states that there can be no long-distance order in a 2D crystal since it is thermodynamically unstable [6, 7]. Geim and his team could isolate samples of a single or a few layers of graphene big enough to enable the study of their properties. They achieved this using simple Scotch tape. Peeling the tape from a graphite sample in a certain way can leave very thin flakes or even a single-layer on it. The question surrounding the Mermin-Wagner theorem have sparked a bit of an argument among researchers, but one possible solution could be spontaneous ripples appearing on free-standing sheets of graphene [8].

Mainly there are three structures of solid state carbon (Fig.:1). These are diamond, fullerenes and graphite [10]. In this work I will focus on the last. The scientific community's interest have been peaked by the novel phenomena observed in structures made of graphene for example anomalous Hall effect [11] or unconventional superconductivity occurring in magic-angle twisted bilayer graphene [12].

Among many other reasons graphene has been in the middle of attention also for its charge carriers. Their behaviour at low energies can be described well, using the (2+1) dimensional zero-mass Dirac equation (named after Paul Dirac [13]). For example this is the reason behind the anomalous Hall effect that I have already mentioned. Massless Dirac fermions were experimentally confirmed in graphene in 2005 [14].

The zoo of two-dimensional materials does not end at graphene. Since the first isolation of it in 2004 numerous other materials were found to have 2D variants with vastly different properties. Even more exotic attributes can be achieved by combining these layers by stacking them on top of each other. Because of the interaction holding them together they were named van der Waals

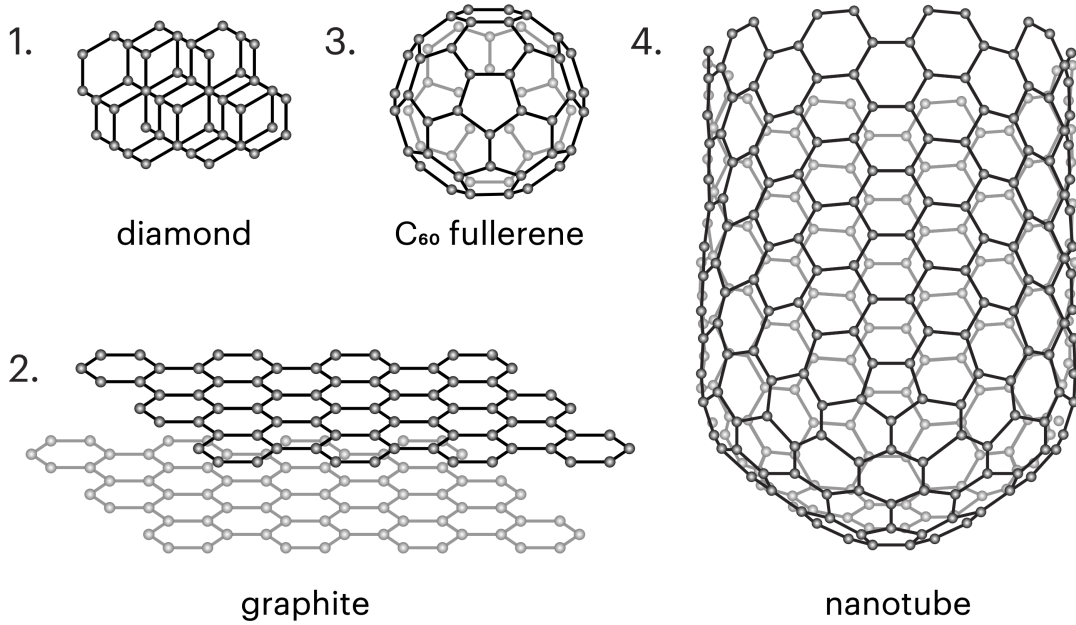


Figure 1: Examples of different allotropes of carbon. Source:[9]

(hetero)structures [15].

Merely stacking graphene layers on top of each other results in a variety of different systems. Such materials are commonly known as few-layer graphene. Even with just two layers, stacking them on top of each other (AA, which is unstable) or stacking them misaligned by a carbon-carbon distance (AB, which is stable) gives very distinct features [16]. As stated by ref.:[17], in nature 80% of graphite is in the stable arrangement of the so called hexagonal (also known as Bernal, named after John Desmond Bernal [18]) structure. Rhombohedral graphite, that makes up for 14%, is a metastable allotrope of the former one that have piqued researchers interest with its novel properties. Among others it has shown semiconducting behaviour with a tunable bandgap [19] and insulating quantum Hall states [20]. It is perhaps the simplest and structurally most perfect condensed matter system to host a flat band protected by symmetry [21]. The last 6% is disordered.

Real-world graphite samples can contain stacking faults, which arise from deviations in the stacking sequence of carbon layers [22]. Due to their profound impact on the material's electronic, mechanical, and optical properties, they play a pivotal role in experimental setups, making them a crucial feature to consider in the design of advanced graphite-based devices.

In my thesis I am going to explore the effect of stacking faults in thin rhombohedral graphite

samples, during which one of my main goals is to create a tool to help in the identification of them. Using a tight binding model I have calculated the projected density of states of different stacking orders which can be compared to their spectra obtained by scanning tunneling microscopy. My tight binding calculations were done in Python.

1.2 Structure of the thesis

After this short introductory chapter I will give a summary of the theoretical background in the second chapter. To begin, I outline a low energy model of graphene that I use as the base of ours. Here, I present the fundamental concepts, definitions and notations used throughout this work. The last part of this chapter is about the physics of scanning tunneling microscopy and its connection to the local density of states. The third chapter introduces the model utilized in this thesis. This section will provide a detailed account of the steps to go from the simple tight binding model of graphene to a system of a few layers with different displacements. The fourth chapter is for the results. I examine the characteristics of the calculated density of states spectra there and describe the machine learning approach for their comparison. The fifth and last chapter includes a summary, a conclusion and future outlook for the thesis.

2 Theoretical background

In this chapter I will summarize the conceptual framework of the description of crystalline materials using their periodicity, geometry and different approximation methods. I will use the tight binding model of graphene to introduce useful definitions such as dispersion relation and density of states. The second subsection includes a description of scanning tunneling microscopy, focusing on the connection between the local density of states and the tunneling current.

2.1 Periodic crystals

A number of materials have crystalline structure in their solid state. These crystals take many different shapes and forms depending on the materials, but they all can be described with a basic unit or tile (if it is the smallest one possible, than it is called the unit cell,) periodically reoccurring in the direction of the lattice vectors $\mathbf{a}_1, \mathbf{a}_2, \mathbf{a}_3$. The whole lattice is translation invariant in the case of displacement by any linear combination of these vectors. This means that we can reach any point of the lattice using the linear combination of these vectors. An infinite system generated from the unit cell by a set of discrete translations is called a Bravais lattice (after Auguste Bravais [23]) and every cell of this lattice has the coordinates:

$$\mathbf{R} = n_1 \mathbf{a}_1 + n_2 \mathbf{a}_2 + n_3 \mathbf{a}_3, \quad (1)$$

where $n_i \in \mathbb{Z}$. This translation symmetry also applies to measurable physical quantities [24]. For the calculation of some of these quantities it is also necessary to define the reciprocal lattice \mathbf{G} and reciprocal lattice vectors $\mathbf{b}_1, \mathbf{b}_2, \mathbf{b}_3$. They respect the following relations:

$$\mathbf{a}_i \mathbf{b}_j = 2\pi \delta_{ij}, \quad (2)$$

where δ_{ij} is the Kronecker delta (named after Leopold Kronecker) and

$$\mathbf{G} = m_1 \mathbf{b}_1 + m_2 \mathbf{b}_2 + m_3 \mathbf{b}_3, \quad (3)$$

where $m_i \in \mathbb{Z}$. The above relations lead to:

$$\mathbf{R}\mathbf{G} = 2\pi i, \quad i \in \mathbb{Z}. \quad (4)$$

As we can identify a unit cell in the real space lattice, so can we choose one in the reciprocal space. A primitive cell is a special unit cell containing only one lattice point. For any given lattice there exists an infinite number of these cells. The primitive cell most commonly chosen is the so called Wigner-Seitz cell (named after Eugene Wigner and Frederick Seitz) [24]. The Brillouin zone (after

Léon Brillouin [25]) can be understood as the Wigner-Seitz cell of the reciprocal lattice (Fig.:2). As we will see later the states of a lattice periodic system can be specified using points of the Brillouin zone.

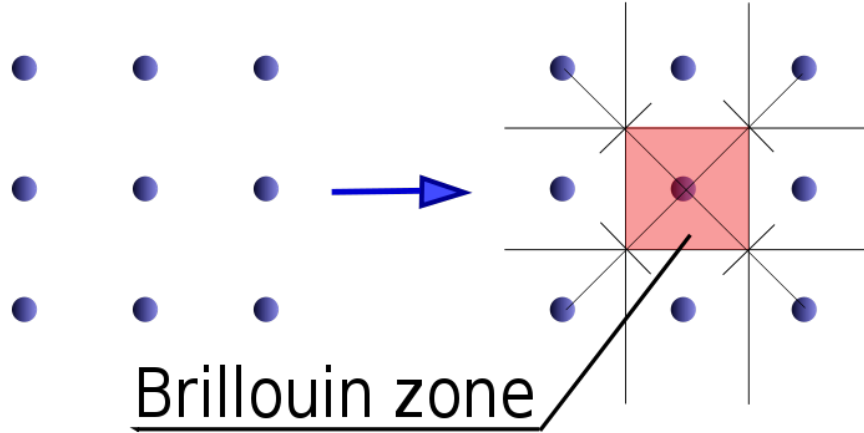


Figure 2: A simple example: the construction of the first Brillouin zone of a square lattice.
Source:[26]

2.2 Tight binding approximation

Describing the behaviour of electrons in a crystal is a great challenge leading to a quantum many-body problem. The properties of this many-body system are given by the Schrödinger equation (named after Erwin Schrödinger [27]), or if we are only interested in the ground state of the system than by the time independent Schrödinger equation:

$$\hat{H}\Psi = E\Psi, \quad (5)$$

where \hat{H} is the Hamilton operator (or Hamiltonian, named after Sir William Rowan Hamilton,) of the system, Ψ is the eigenfunction and E is the eigenenergy. For a system of more than a few atoms it is impossible to solve this equation analytically and numerical solutions are very costly and can only be done on supercomputers [28, 29].

The next best approach is to use approximations. Max Born and J. Robert Oppenheimer proposed that due to the significant difference between the mass of atomic nuclei and that of electrons, the nuclei can be regarded as stationary from the electron's point of view [30]. This way the solution of the Schrödinger equation (eq.:(5)) can be factored as the multiple of the separate wave functions of electrons and ions.

The electrons interact with each other via the Coulomb interaction (named after Charles-Augustin

de Coulomb [31]), which is repulsive and infinite range. This means that each electron is affected by every other. To account for this effect, we would need to compute a huge number of pair interactions, which is extremely costly. A solution to this problem is to imagine that every electron is moving in a mean field induced by all the other electrons. This approximation leads back to the problem of only one electron in a potential $U_{el}(\mathbf{r})$. The above-mentioned potential must respect translation symmetry and therefore be lattice periodic: $U_{el}(\mathbf{r}) = U_{el}(\mathbf{r} + \mathbf{R})$. According to Bloch's theorem (discovered by Felix Bloch in 1929 [32]) the solutions of the Schrödinger equation in a periodic potential are plane waves with a periodic modulation. They can be written in the form:

$$\psi_{\mathbf{k}} = e^{i\mathbf{kr}} u(\mathbf{r}), \quad (6)$$

where $\psi_{\mathbf{k}}$ is the wave function of the electron, \mathbf{k} is a wave vector (i.e.: momentum vector) and $u(\mathbf{r})$ is an arbitrary function with lattice periodicity: $u(\mathbf{r}) = u(\mathbf{r} + \mathbf{R})$.

The tight binding method was first suggested by Felix Bloch, then John Clarke Slater and George Fred Koster further simplified it [33]. It incorporates the approximations above, describing the system on the basis of the wave functions of electrons bound to atoms. In this way the strongest effect on the electron comes from the atom it is bound to and the effect of other ions can be regarded as a perturbation. The Hamiltonian of the system is built as a sum:

$$\hat{H} = \hat{H}_0 + \Delta U, \quad (7)$$

where \hat{H}_0 is the Hamiltonian of a single atom and ΔU is the difference between the potential of a single atom and that of the whole crystal. The atomic orbitals are functions localized to the atomic positions with vanishing probabilities at other atoms. They can be obtained from the Schrödinger equation:

$$\hat{H}_0 \phi_i(\mathbf{r}) = \epsilon_i \phi_i(\mathbf{r}), \quad (8)$$

where ϵ_i is the i^{th} energy level of an atom. The wave functions of electrons must respect Bloch's theorem, which is not true for the atomic orbitals. We can define such functions using the linear combination of the atomic orbitals:

$$\psi_{n,\mathbf{k}}(\mathbf{r}) = \frac{1}{\sqrt{N}} \sum_{\mathbf{R}} e^{i\mathbf{kr}} \phi_n(\mathbf{r} - \mathbf{R}), \quad (9)$$

where N is the number of unit cells in the lattice and the l index indicates them. The Bloch theorem can easily be verified by shifting the wave function by the translation vector \mathbf{R}' :

$$\begin{aligned}\psi_{n,\mathbf{k}}(\mathbf{r} + \mathbf{R}') &= \frac{1}{\sqrt{N}} \sum_{\mathbf{R}} e^{i\mathbf{k}(\mathbf{R} + \mathbf{R}' - \mathbf{R}')} \phi_n(\mathbf{r} + \mathbf{R}' - \mathbf{R}) \\ &= e^{i\mathbf{k}\mathbf{R}'} \frac{1}{\sqrt{N}} \sum_{\mathbf{R}} e^{i\mathbf{k}(\mathbf{R} - \mathbf{R}')} \phi_n(\mathbf{r} - (\mathbf{R} - \mathbf{R}')) \\ &= e^{i\mathbf{k}\mathbf{R}'} \psi_{n,\mathbf{k}}(\mathbf{r}).\end{aligned}\quad (10)$$

Utilizing the property that the difference of two lattice translation vectors is also a lattice translation vector.

The wave function describing the whole crystal can be expanded on the basis of these wave functions:

$$\psi_{\mathbf{k}}(\mathbf{r}) = \sum_j c_{\mathbf{k},j} \psi_{j,\mathbf{k}}(\mathbf{r}), \quad (11)$$

where $c_{\mathbf{k},j}$ denotes the coefficients of the linear combination. To find these coefficients we have to take into consideration the variational principle, which states that the best approximation minimizes the expectation value of the energy. After rearranging the Schrödinger equation and acting with the complex conjugated wave function from the left:

$$\sum_{i,j} c_{\mathbf{k},i}^* c_{\mathbf{k},j} \left(\int d\mathbf{r} \psi_{i,\mathbf{k}}^*(\mathbf{r}) \hat{H} \psi_{j,\mathbf{k}}(\mathbf{r}) - \epsilon_{\mathbf{k}} \int d\mathbf{r} \psi_{i,\mathbf{k}}^*(\mathbf{r}) \hat{H} \psi_{j,\mathbf{k}}(\mathbf{r}) \right) = 0. \quad (12)$$

Substituting in eq.: (9) defines:

$$H_{i,j}(\mathbf{k}) = \frac{1}{N} \sum_{\mathbf{R}, \mathbf{R}'} e^{i\mathbf{k}(\mathbf{R} - \mathbf{R}')} \int d\mathbf{r} \phi_i^*(\mathbf{r} - \mathbf{R}') \hat{H}(\mathbf{r} - \mathbf{R}) \phi_j(\mathbf{r} - \mathbf{R}), \quad (13)$$

the hopping integral and:

$$S_{i,j}(\mathbf{k}) = \frac{1}{N} \sum_{\mathbf{R}, \mathbf{R}'} e^{i\mathbf{k}(\mathbf{R} - \mathbf{R}')} \int d\mathbf{r} \phi_i^*(\mathbf{r} - \mathbf{R}') \phi_j(\mathbf{r} - \mathbf{R}), \quad (14)$$

the overlap integral. These integrals are usually very complicated, therefore the values are often left as parameters, which can be obtained for example by fitting to density functional theory calculations [34]. The $c_{\mathbf{k},j}$ coefficients are obtained with variational method:

$$\epsilon_{\mathbf{k}} = \frac{\sum_{i,j} H_{i,j}(\mathbf{k}) c_{\mathbf{k},i}^* c_{\mathbf{k},j}}{\sum_{i,j} S_{i,j}(\mathbf{k}) c_{\mathbf{k},i}^* c_{\mathbf{k},j}}, \quad (15)$$

to minimize energy the coefficients should be chosen so that:

$$\frac{\partial \epsilon_{\mathbf{k}}}{\partial c_{\mathbf{k},i}^*} = 0. \quad (16)$$

This leads to:

$$\sum_j [H_{i,j}(\mathbf{k}) - \epsilon_{\mathbf{k}} S_{i,j}(\mathbf{k})] c_{\mathbf{k},j} = 0. \quad (17)$$

The energy spectrum is given by the solution of eq.: (17). Usually it is more convenient to use an orthogonal basis, in which the off-diagonal elements of the overlap matrix are assumed to be zero: $S_{i,j} = \delta_{i,j}$. Henceforth we will look at systems, in which this assumption holds true. This means that the energy levels are equal to the eigenvalues of $H_{i,j}$. In the next section the application of this method is explored through the well-known example of graphene.

2.3 Tight binding description of graphene

This section is based on the doctoral dissertation of my supervisor Zoltán Tajkov [35] and the DSc thesis of József Cserti [36]. Graphene is a honeycomb lattice with two equivalent carbon atoms in each unit cell (Fig.:3). They can be denoted as A and B. Both A and B atoms form a triangular lattice on their own. As it is a 2D structure it has two lattice vectors, we will choose them in the following way:

$$\mathbf{a}_1 = \frac{a_{cc}}{2} \begin{pmatrix} -\sqrt{3} \\ 3 \end{pmatrix} \quad \mathbf{a}_2 = \frac{a_{cc}}{2} \begin{pmatrix} \sqrt{3} \\ 3 \end{pmatrix}, \quad (18)$$

where a_{cc} is the distance between neighbouring carbon atoms, approximately $a_{cc} \approx 1.42\text{\AA}$ [37].

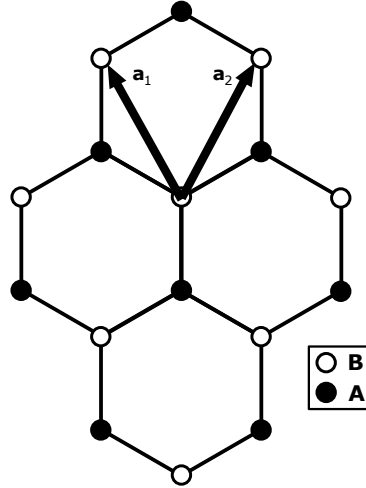


Figure 3: The hexagonal lattice with the lattice vectors. The empty and filled circles mark the sublattices B and A accordingly.

The corresponding reciprocal lattice vectors come from eq.: (2):

$$\mathbf{b}_1 = \frac{2\pi}{3a_{cc}} \begin{pmatrix} -\sqrt{3} \\ 1 \end{pmatrix}, \quad \mathbf{b}_2 = \frac{2\pi}{3a_{cc}} \begin{pmatrix} \sqrt{3} \\ 1 \end{pmatrix}. \quad (19)$$

In graphene the atomic orbitals of electrons hybridize into sp^2 hybrid states forming the σ -bonds. These are equivalent bonds with the three nearest neighbours. The 4th electron of each atom occupies the p_z orbital perpendicular to the plane forming the π -bonds (see Fig.:4).

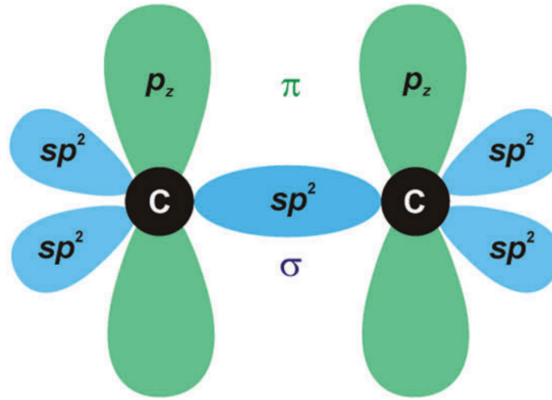


Figure 4: sp^2 hybridization of atomic orbitals in graphene. Source:[38]

For the tight binding description we will only take π -bonds and nearest neighbour interactions into account. We can denote one particle states as:

$$|\alpha, \mathbf{R}\rangle = |\alpha\rangle \otimes |\mathbf{R}\rangle, \quad |A\rangle = \begin{pmatrix} 1 \\ 0 \end{pmatrix}, \quad |B\rangle = \begin{pmatrix} 0 \\ 1 \end{pmatrix}, \quad (20)$$

where \mathbf{R} is defined the same as in eq.: (1) and $\alpha = A, B$ indicates the sublattice point. The real-space Hamiltonian can be formulated using these notations as:

$$\hat{H} = \gamma_0 \sum_{\mathbf{R}} |B, \mathbf{R}\rangle \langle A, \mathbf{R}| + |B, \mathbf{R}\rangle \langle A, \mathbf{R} + \mathbf{a}_1| + |B, \mathbf{R}\rangle \langle A, \mathbf{R} + \mathbf{a}_2| + h.c., \quad (21)$$

where γ_0 is the hopping integral, which can be arbitrarily chosen, but $\gamma_0 \approx 2.7\text{eV}$ is commonly found in scientific literature [39].

To calculate the dispersion relation and electric band structure of graphene we require the \mathbf{k} dependent (also known as: momentum-space) Hamiltonian. It can be obtained through Fourier transformation (named after Jean-Baptiste Joseph Fourier [40]) using the translation invariance of

the lattice. The transformations are defined in the following manner:

$$\begin{aligned} |B, \mathbf{R}\rangle &= \frac{1}{\sqrt{N}} \sum_{\mathbf{k}} e^{i\mathbf{k}\mathbf{R}} |B, \mathbf{k}\rangle, \\ |A, \mathbf{R}\rangle &= \frac{1}{\sqrt{N}} \sum_{\mathbf{k}} e^{i\mathbf{k}\mathbf{R}} |A, \mathbf{k}\rangle, \end{aligned} \quad (22)$$

where N is the number of unit cells. Substituting these definitions into eq.: (21) yields the \mathbf{k} dependent Hamiltonian. The first term can be brought to this form:

$$\begin{aligned} \sum_{\mathbf{R}} |B, \mathbf{R}\rangle \langle A, \mathbf{R}| &= \frac{1}{N} \sum_{\mathbf{R}} \sum_{\mathbf{k}, \mathbf{k}'} e^{i\mathbf{k}\mathbf{R}} e^{-i\mathbf{k}'\mathbf{R}} |B, \mathbf{k}\rangle \langle A, \mathbf{k}'| \\ &= \frac{1}{N} \sum_{\mathbf{R}} \sum_{\mathbf{k}, \mathbf{k}'} e^{i(\mathbf{k}-\mathbf{k}')\mathbf{R}} |B, \mathbf{k}\rangle \langle A, \mathbf{k}'|. \end{aligned} \quad (23)$$

Upon closer inspection of the summation over \mathbf{R} we can recognise an important property.

$$\sum_{\mathbf{R}} e^{i(\mathbf{k}-\mathbf{k}')\mathbf{R}} = \sum_{n_1=1}^{N_1} \sum_{n_2=1}^{N_2} e^{i\Delta\mathbf{k}(n_1\mathbf{a}_1 + n_2\mathbf{a}_2)}, \quad (24)$$

using the definition of R , $N_1 \cdot N_2 = N$ and $\Delta\mathbf{k} = \mathbf{k} - \mathbf{k}'$. $\Delta\mathbf{k}$ can be expressed on the basis of the reciprocal lattice vectors as: $\Delta\mathbf{k} = \Delta k_1 \mathbf{b}_1 + \Delta k_2 \mathbf{b}_2$, where $\Delta k_i = \frac{m}{N_i}$ with $m = 0 \dots N_i - 1$. Substituting this into eq.: (24) an important property can be recognised:

$$\sum_{\mathbf{R}} e^{i(\mathbf{k}-\mathbf{k}')\mathbf{R}} = \sum_{n_1}^{N_1} e^{2\pi i n_1 \Delta k_1} \sum_{n_2}^{N_2} e^{2\pi i n_2 \Delta k_2} = N_1 \delta_{\Delta k_1, 0} \cdot N_2 \delta_{\Delta k_2, 0} \quad (25)$$

where we utilized eq.: (2). This comes from the summation of a geometric series:

$$\sum_{n_j}^{N_j} e^{2\pi i n_j \Delta k_j} = \frac{(-1 + e^{2\pi i \Delta k_j}) e^{2\pi i \frac{\Delta k_j}{N_j}}}{-1 + e^{2\pi i \frac{\Delta k_j}{N_j}}} = N_j \delta_{\Delta k_j, 0}. \quad (26)$$

The Kronecker delta $\delta_{\Delta k_j, 0}$ means that eq.: (25) is only non-zero if both Δk_1 and Δk_2 are zero. This implies that $\Delta\mathbf{k}$ must be zero and therefore eq.: (23) simplifies to:

$$\sum_{\mathbf{R}} |B, \mathbf{R}\rangle \langle A, \mathbf{R}| = \sum_{\mathbf{k}} |B, \mathbf{k}\rangle \langle A, \mathbf{k}|. \quad (27)$$

The other terms of eq.: (21) can also be transformed in the same manner as above:

$$\begin{aligned} \sum_{\mathbf{R}} |B, \mathbf{R}\rangle \langle A, \mathbf{R} + \mathbf{a}_1| &= \frac{1}{N} \sum_{\mathbf{R}} \sum_{\mathbf{k}, \mathbf{k}'} e^{i\mathbf{k}\mathbf{R}} e^{-i\mathbf{k}'(\mathbf{R} + \mathbf{a}_1)} |B, \mathbf{k}\rangle \langle A, \mathbf{k}'| \\ &= \frac{1}{N} \sum_{\mathbf{R}} \sum_{\mathbf{k}, \mathbf{k}'} e^{i(\mathbf{k}-\mathbf{k}')\mathbf{R}} e^{-i\mathbf{k}'\mathbf{a}_1} |B, \mathbf{k}\rangle \langle A, \mathbf{k}'|. \end{aligned} \quad (28)$$

The Kronecker delta appears in these terms with an additional exponential term containing the lattice vector, that can be regarded as a phase factor. The final forms of the transformations are obtained through the same steps as described above. They are the following:

$$\sum_{\mathbf{R}} |B, \mathbf{R}\rangle \langle A, \mathbf{R} + \mathbf{a}_1| = \sum_{\mathbf{k}} e^{-i\mathbf{k}\mathbf{a}_1} |B, \mathbf{k}\rangle \langle A, \mathbf{k}|, \quad (29)$$

$$\sum_{\mathbf{R}} |B, \mathbf{R}\rangle \langle A, \mathbf{R} + \mathbf{a}_2| = \sum_{\mathbf{k}} e^{-i\mathbf{k}\mathbf{a}_2} |B, \mathbf{k}\rangle \langle A, \mathbf{k}|. \quad (30)$$

The momentum-space Hamiltonian of the system takes the form:

$$\hat{H} = \gamma_0 \sum_{\mathbf{k}} f(\mathbf{k}) |B, \mathbf{k}\rangle \langle A, \mathbf{k}| + h.c., \quad (31)$$

where $f(\mathbf{k})$ comes from the phase factors:

$$f(\mathbf{k}) = 1 + e^{-i\mathbf{k}\mathbf{a}_1} + e^{-i\mathbf{k}\mathbf{a}_2}. \quad (32)$$

After choosing a basis vector $\underline{\Psi}_{\mathbf{k}} = (|B, \mathbf{k}\rangle, |A, \mathbf{k}\rangle)$ we can rewrite eq.: (31) in a matrix form:

$$\hat{H} = \gamma_0 \sum_{\mathbf{k}} \underline{\Psi}_{\mathbf{k}} \begin{pmatrix} 0 & f(\mathbf{k}) \\ f^*(\mathbf{k}) & 0 \end{pmatrix} \underline{\Psi}_{\mathbf{k}}^\dagger. \quad (33)$$

The tight binding modell is now represented with the matrix:

$$\mathbf{H}(\mathbf{k}) = \gamma_0 \begin{pmatrix} 0 & f(\mathbf{k}) \\ f^*(\mathbf{k}) & 0 \end{pmatrix}. \quad (34)$$

The dispersion relation of graphene is given by the eigenvalues of this matrix:

$$E(\mathbf{k}) = \pm \gamma_0 |f(\mathbf{k})| = \pm \gamma_0 \sqrt{3 + 2 \cos(\mathbf{k}\mathbf{a}_1) + 2 \cos(\mathbf{k}\mathbf{a}_2) + 2 \cos(\mathbf{k}(\mathbf{a}_1 - \mathbf{a}_2))}. \quad (35)$$

The band structure (Fig.:5) is the dispersion relation calculated at the points of the Brillouin zone. It is worth mentioning that the band structure is symmetric to zero energy, which originates from the chiral symmetry (also known as sublattice symmetry) of graphene [41]. Another prominent feature is the six Dirac cones at the \mathbf{K} points of the Brillouin zone. At these points the valence bands and conduction bands meet in a single point called the Dirac point. Of these six there are two that can be chosen, so that they are not equivalent to each other. They are often denoted as \mathbf{K} and \mathbf{K}' and can be:

$$\mathbf{K} = \frac{2\mathbf{b}_1 + \mathbf{b}_2}{3}, \quad \mathbf{K}' = \frac{2\mathbf{b}_2 + \mathbf{b}_1}{3}. \quad (36)$$

Substituting these \mathbf{k} values into eq.: (35) gives zero showing that the bands touch. As we are mostly interested in the low energy regime it is useful to do a Taylor expansion (named after Brook Taylor

[42]) of the dispersion relation around the Dirac points. This way we get a linear relation for the energy. (This is also the reason for the cone shape.)

$$E(\mathbf{k}) = \pm \hbar v |\mathbf{k}|, \quad (37)$$

where \hbar is the reduced Planck's constant (named after Max Planck [43]) and $\hbar v = \gamma_0 \cdot a_{cc} \cdot 3/2$.

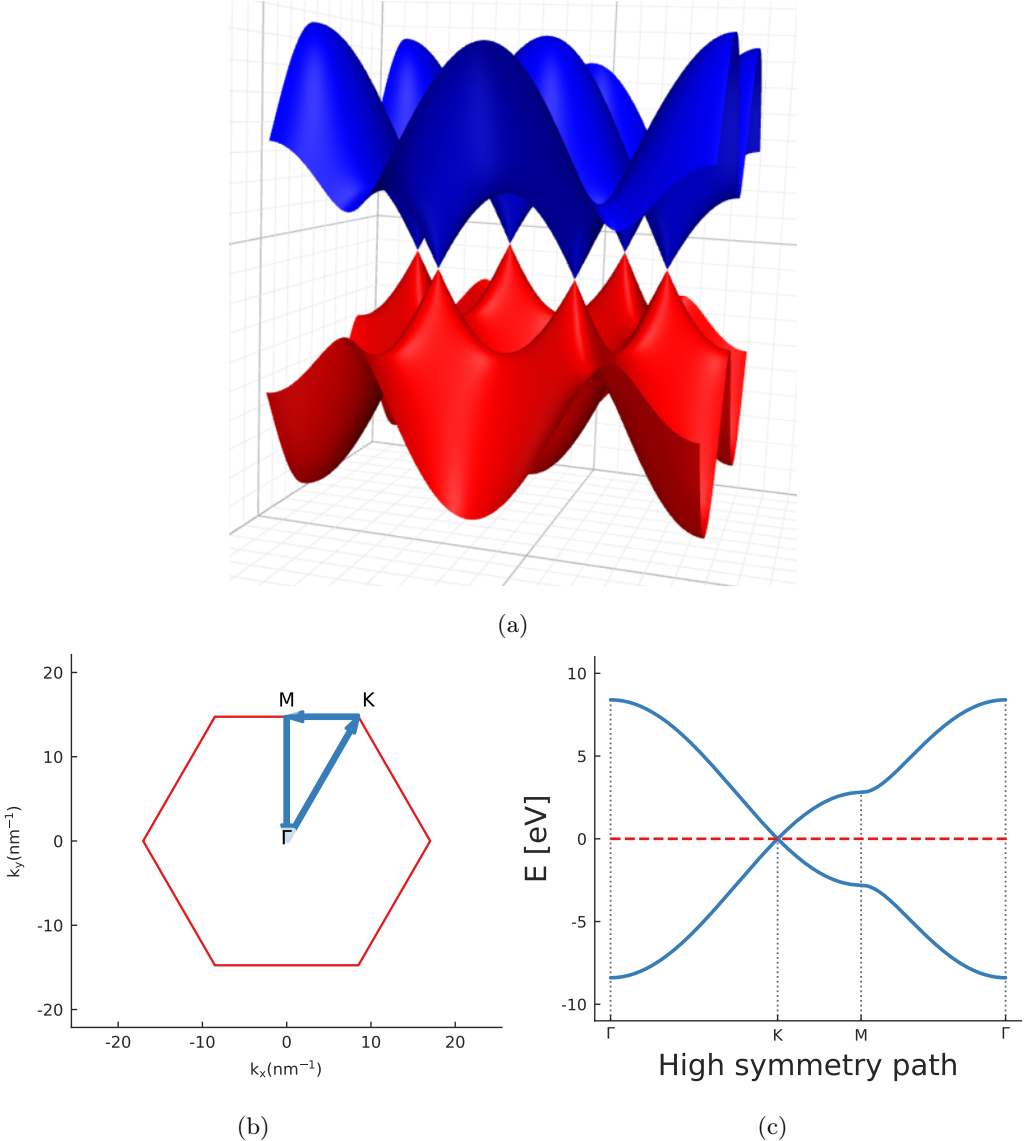


Figure 5: (a) The six Dirac cones of the Brillouin zone of graphene. The conduction band is coloured blue and the valence band red. (b) A high symmetry path commonly taken in the sampling of the Brillouin zone: $\Gamma \rightarrow \mathbf{K} \rightarrow \mathbf{M} \rightarrow \Gamma$. (c) The band structure of graphene. The red dashed line indicates the Fermi energy.

2.4 Density of states

2.4.1 Density of states of graphene

The density of states (DOS) describes the number of states per unit volume per unit energy. It is defined as:

$$D(E) = \frac{1}{A} \sum_{j=1}^N \delta(E - E(\mathbf{k}_j)), \quad (38)$$

where $\delta(E - E(\mathbf{k}_j))$ is the Dirac delta and we use the area A instead of the volume because of the 2D lattice. N is the number of \mathbf{k}_j vectors in the Brillouin zone. These vectors can be expressed as: $\mathbf{k} = (k_x, k_y)$. Taking a finite sample with Born–von Kármán boundary condition [24], (named after Max Born and Theodore von Kármán) the number of possible vectors is given by:

$$k_x = \frac{2\pi}{L_x} m_x, \quad k_y = \frac{2\pi}{L_y} m_y, \quad (39)$$

where $L_x \cdot L_y = A$ and $m_x, m_y \in \mathbb{Z}$. The reason behind the discrete set of vectors is that the wavelength of plane waves chosen as the states of the electrons (see eq.: (6)) must fit the lattice in each direction an integer number of times.

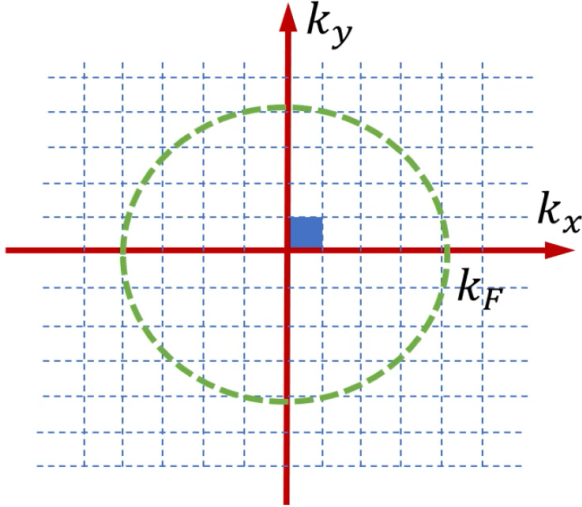


Figure 6: The momentum-space coordinate system. Area occupied by each state is indicated in blue. The green circle represents momenta corresponding to the Fermi energy.

At zero temperature the electron density n is given by integrating the DOS from zero to the Fermi energy (named after Enrico Fermi):

$$n(E_F) = \int_0^{E_F} D(E) dE. \quad (40)$$

We can also gather this value by counting the total number of states in the circle of k_F radius in the momentum-space as seen in Fig.:6. Each state occupies an area:

$$a = k_x \cdot k_y = \frac{4\pi}{L_x L_y}. \quad (41)$$

Then the total number of electrons is given by the amount of states in the circle:

$$N = \frac{\pi k_F^2}{a} = \frac{k_F^2 L_x L_y}{4\pi}. \quad (42)$$

Now the electron density is the total number of electrons divided by the area of the system:

$$n = \frac{N}{L_x L_y} \cdot g = \frac{k_F^2}{\pi}, \quad (43)$$

where $g = 4$ because of the spin of the electrons and the two valleys coming from the two atoms in each unit cell. The DOS can be expressed from eq.:(40) as a derivative taken at the Fermi energy:

$$D(E_F) = \left. \frac{dn}{dE} \right|_{E_F} = \left. \frac{d}{dE} \left(\frac{E^2}{\pi \hbar^2 v^2} \right) \right|_{E_F} = \frac{2}{\pi \hbar^2 v^2} |E_F|, \quad (44)$$

where we substituted in eq.:(37) for k_F . Eq.:(44) shows a linear relation in the case of energies near the Fermi energy. This can be seen in Fig.:7. We will stay in this regime for the remainder of the thesis.

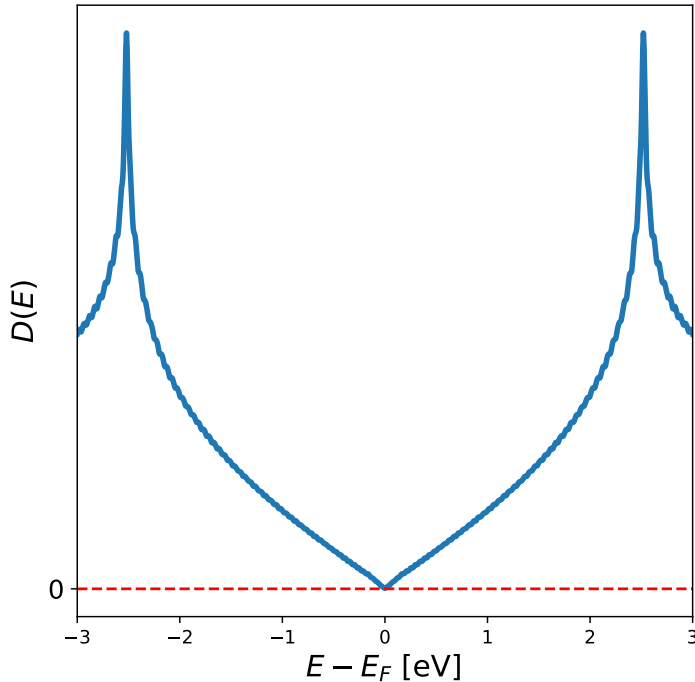


Figure 7: Density of states of a graphene monolayer.

2.4.2 Projected density of states and numerical calculations

In the case of a system with more atoms in its unit cell eq.:(38) needs an additional summation over the bands:

$$D(E) = \frac{1}{N_{\mathbf{k}}} \sum_i^{\text{bands}} \sum_{j=1}^N \delta(E - E_i(\mathbf{k}_j)), \quad (45)$$

where now N_k is the number of all possible states. In later sections the projected density of states (PDOS) is often used. It is similar to the local density of states (LDOS), but while LDOS gives the DOS on a certain real-space point of the system, PDOS gives the DOS weighted to each eigenstate. In our tight binding model we choose these states to be localized to lattice points thus PDOS is the same as LDOS.

$$\text{PDOS}_n(E) = \frac{1}{A} \sum_i^{\text{bands}} \sum_{j=1}^N |\Psi_n(\mathbf{k})|^2 \delta(E - E_i(\mathbf{k}_j)). \quad (46)$$

The following relation holds true for PDOS and DOS:

$$D(E) = \sum_n \text{PDOS}_n(E). \quad (47)$$

A problem arises from the Dirac delta, namely it cannot be used in numerical calculations. The solution to this is to introduce a function with similar properties. This function is the Gaussian function (named after Johann Carl Friedrich Gauss):

$$\delta(E - E_i(\mathbf{k})) \rightarrow \frac{\mathfrak{N}}{\alpha\sqrt{\pi}} e^{-\frac{(E - E_i(\mathbf{k}))^2}{\alpha^2}}, \quad (48)$$

where \mathfrak{N} is a normalization factor and α tunes the width of the bell curve thus it can be regarded as a smoothing factor. The bigger it is the more each $E_i(\mathbf{k})$ can contribute to the DOS evaluated at the E energies, making the resulting curves smoother (see Fig.:8). The cost of this smoothing is that only those features can be distinguished from each other, which are at least α distance from each other in energy.

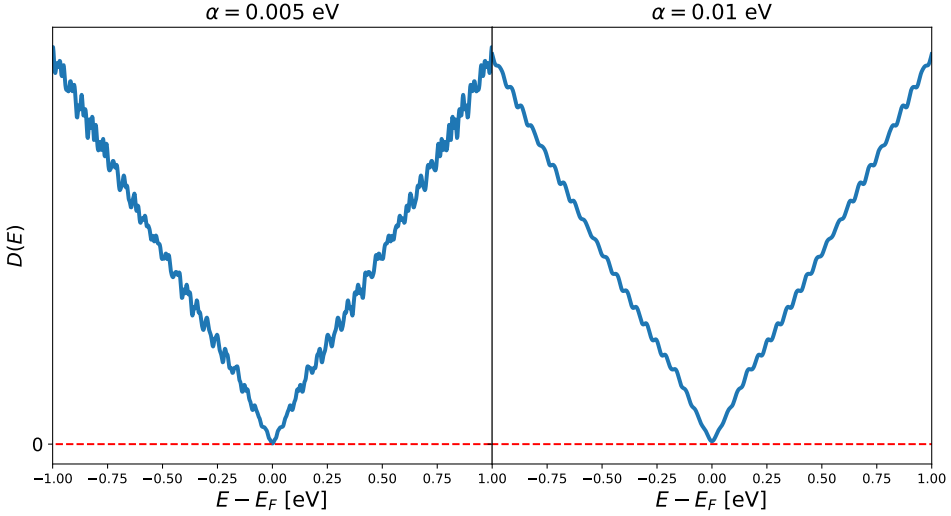


Figure 8: The effect of α on the smoothness of the DOS.

2.5 Scanning tunneling microscopy and its connection to LDOS

2.5.1 The scanning tunneling microscope

The first successful tunneling experiment through a vacuum gap was reported by Gerd Binnig et al., 1982 [44]. Gerd Binnig and Heinrich Rohrer was awarded the Nobel Prize in Physics for the design of the scanning tunneling microscope (STM) in 1986. Since then scanning tunneling microscopy has become a widely utilized imaging technique. This method offers the possibility of direct, real-space determination of surface structure in three dimensions and also for non-periodic structures [45, 46]. The setup of an STM device is illustrated in Fig.:9. An atomically thin tip attached to a piezoelectric tube is moved across the sample. If the tip is lowered close enough ($\leq 1 \text{ nm}$) to the surface a tunneling current appears at a set bias voltage. While moving the tip by adjusting the voltage applied to the piezoelectric tube, the sample can be scanned in a very high resolution. Lateral resolution can reach $\sim 1 \text{\AA}$ and vertical resolution can be as good as $\sim 0.1 \text{\AA}$.

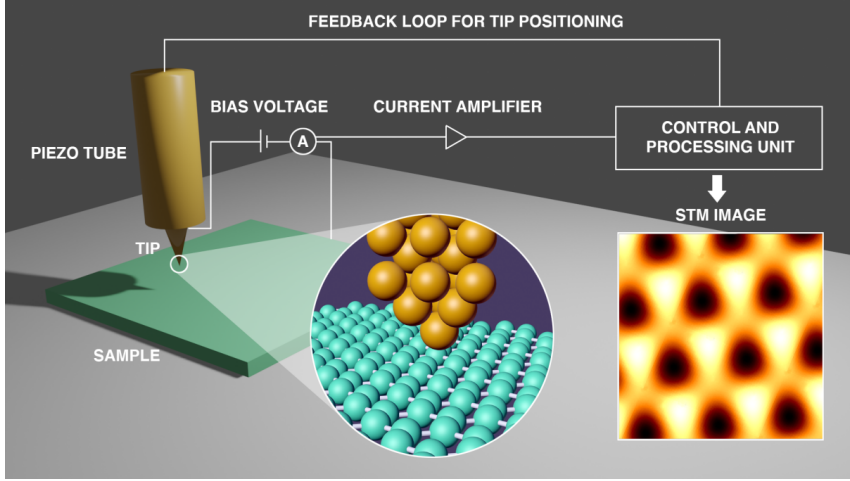


Figure 9: Schematic view of an STM device. Source:[47]

It is important to point out that STM does not only image the geometry of the surface, but the combination of the atomic geometry and the convolution of the electron DOS of the sample and that of the tip. In this thesis we are most interested in the electron DOS of the sample, therefore in the next subsection we will look at the theoretical background of these measurements.

2.5.2 Theoretical description of STM

The theoretical description of STM was proposed by J. Tersoff and D.R. Hamann [48]. In this subsection I will follow their train of thought to show the connection between STM and LDOS. The tunneling current is given to first order in Bardeen's formalism (published by John Bardeen [49]) as:

$$I = \frac{2\pi e}{\hbar} \sum_{\mu,\nu} f(E_\mu)[1 - f(E_\nu - eV)] |M_{\mu\nu}|^2 \delta(E_\mu - E_\nu), \quad (49)$$

where $f(E)$ is the Fermi function, V is the applied voltage, e is the elementary charge, $E_{\mu/\nu}$ is the energy of the states of the probe/surface. $M_{\mu\nu}$ is the tunneling matrix element between states of the probe ψ_μ and the surface ψ_ν :

$$M_{\mu\nu} = \frac{\hbar^2}{2m} \int d\mathbf{S} (\psi_\mu^* \nabla \psi_\nu - \psi_\nu \nabla \psi_\mu^*), \quad (50)$$

where \mathbf{S} is the normal vector of any surface lying entirely within the vacuum barrier between the tip and surface. Since the experiments are performed at room temperature or below and with small voltages we can take the limiting case of small temperature and voltage of eq.:(49):

$$I = \frac{2\pi e^2 V}{\hbar} \sum_{\mu,\nu} |M_{\mu\nu}|^2 \delta(E_\nu - E_F) \delta(E_\mu - E_F). \quad (51)$$

This result comes from the properties of the Fermi function, since at $T = 0$ eq.: (49) can only be non-zero if both E_μ and E_ν are equal to the Fermi energy. Another simplification is to consider the probe tip to be point-like and its wave functions to be arbitrarily localized. This way the tunneling matrix element is simply proportional to the amplitude of the surface wave function at the \mathbf{r}_0 position of the probe. This results in:

$$I \propto \sum_{\nu} |\psi_{\nu}(\mathbf{r}_0)|^2 \delta(E_{\nu} - E_F). \quad (52)$$

The quantity on the right hand side is the surface LDOS at the Fermi energy. The tunneling current is proportional to the surface LDOS at \mathbf{r}_0 , therefore the STM image can be compared to LDOS calculations. To get a more general expression we would have to account for the shape of the probe and that the probe wave function cannot be localized to a point, but for the scope of this thesis it is enough that we see the connection between STM and LDOS.

3 Rhombohedral graphite and stacking faults

The study of stacking faults in rhombohedral graphite have piqued the scientific community's interest for years. Stacking order has a profound effect on the electric structure of the samples that is actively studied both theoretically and experimentally [50, 51, 52].

In graphite crystals, layers of graphene reside in three equivalent, but distinct, stacking positions typically referred to as A, B, and C. This can be used to denote the different structures. We shall have a look at three different arrangements of a trilayer sample of graphene. These are AAA, ABA and ABC. Fig.:10 shows the band structure of them. AAA has three distinct Dirac cones, one in the **K** point and the other two displaced. ABA has a structure containing both a linear Dirac cone and two quadratic dispersion bands that is indicative of the structure of an AB bilayer. Lastly, ABC has a flat band at the Fermi energy. This will result in a very high DOS at that energy, which provides new opportunities for realizing many exotic properties, e.g. flat band high temperature superconductivity [53].

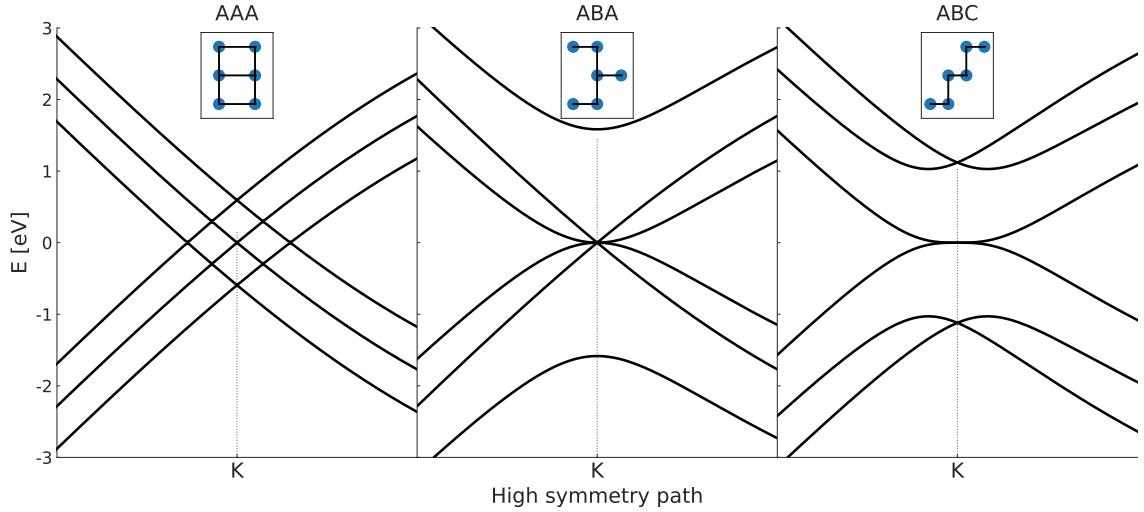


Figure 10: The band structures of different stacking configurations. The inset pictures depict the carbon atoms of the unit cell of each layer and the first neighbours are connected with black lines.

As the number of layers grows, so do the possible sequences that the layers can be arranged in. After the bottom layer each layer could occupy three positions: displaced to the right/left or directly on top. This means $n = 3^{N-1}$ combinations, where N is the number of layers, but many of these are not topologically different from each other and can be rotated or mirrored so that they are the same. Their band structure and DOS is also the same, thus it is not necessary to compute every combination. In the next section we shall see how to choose all the topologically different

combinations. As it turns out most of the sequences can be dropped, lowering the computational time significantly.

3.1 What are the possible stacking configurations?

As mentioned above, there is a huge number of sequences that a graphite sample can be arranged in. Our aim is to calculate the DOS of only those that are topologically different, since that is enough to identify any measured sample.

But first, we shall drop any structure containing an AA sequence. The reason for that is a small energy barrier between AA and AB stacking, which makes the former unstable. Fig.:11 shows how much energy is needed to shift the top layer of Bernal graphite to ABC or AA configurations. With this consideration the number is down to $n = 2^{N-1}$, while the next layer is always displaced either to the left or right.

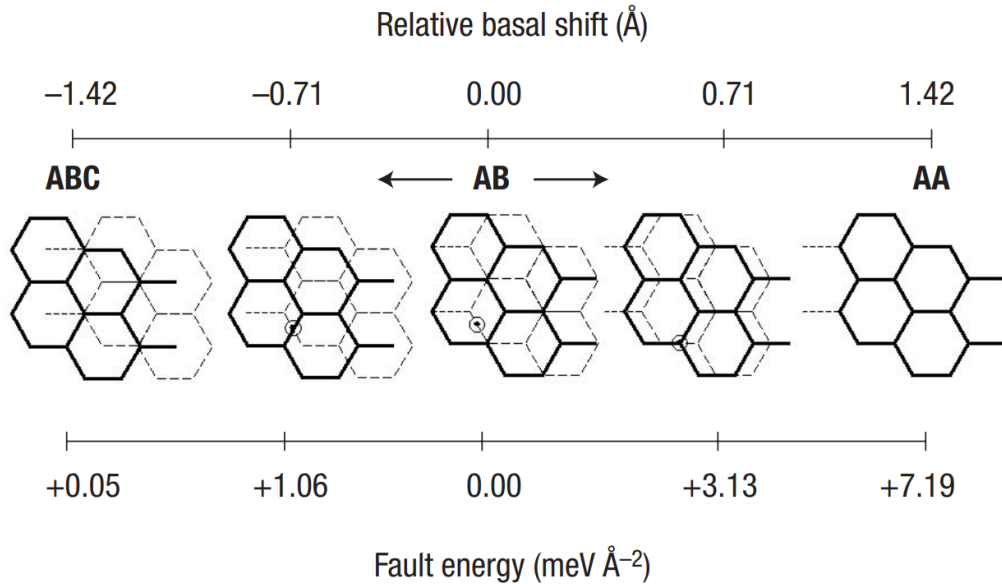


Figure 11: The energy difference between ABC and AA on top of Bernal graphite. Source:[54]

To get all different structures let us start building up from the thinnest. With $N = 2$ there is only one configuration AB after excluding the mirror image. In the case of $N = 3$ there are two possibilities ABA and ABC. These are very easy to see, so I will detail the train of thought with the example of $N = 4$.

The first layer is always fixed. Thereafter, every layer can either go to the left or the right hand side of the previous one. We will denote them "-1" and "+1" accordingly. This way any configuration

can be given by a sequence of " -1 "s and " $+1$ "s with length $N - 1$. For example:

$$\begin{aligned} \text{ABA} &\Rightarrow +1 - 1, \\ \text{ABC} &\Rightarrow +1 + 1. \end{aligned} \tag{53}$$

Changing every " $+1$ " into a " -1 " and vice versa yields the horizontal mirror images, thus:

$$\begin{aligned} \text{ABA} &\Rightarrow +1 - 1 = -1 + 1, \\ \text{ABC} &\Rightarrow +1 + 1 = -1 - 1. \end{aligned} \tag{54}$$

Because of this symmetry only those sequences should be accounted for that have a maximum of $n_- = \lfloor (N - 1)/2 \rfloor$ " $-$ " signs, where $\lfloor \cdot \rfloor$ is the symbol of the floor function. Another symmetry is flipping the order of the sequence. A flipped sequence gives the vertical mirror image of the original one. Every time we do our calculations on a configuration we get both the top and bottom PDOS, consequently those duplicates can also be dropped. Using these restrictions the valid configurations for $N = 4$ can be seen in Fig.:12.

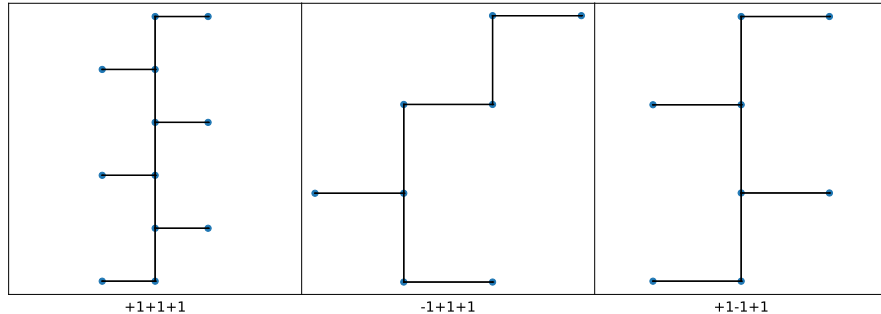


Figure 12: All three topologically different configurations of four-layer systems.

As we can see, removing the unnecessary structures significantly lowers the amount of calculations, thus reducing computational time. The number of calculations needed as the function of thickness can be seen in Fig.:13. As an example $N = 10$ has all together 19683, without AA stacking 512 and only 136 topologically different combinations.

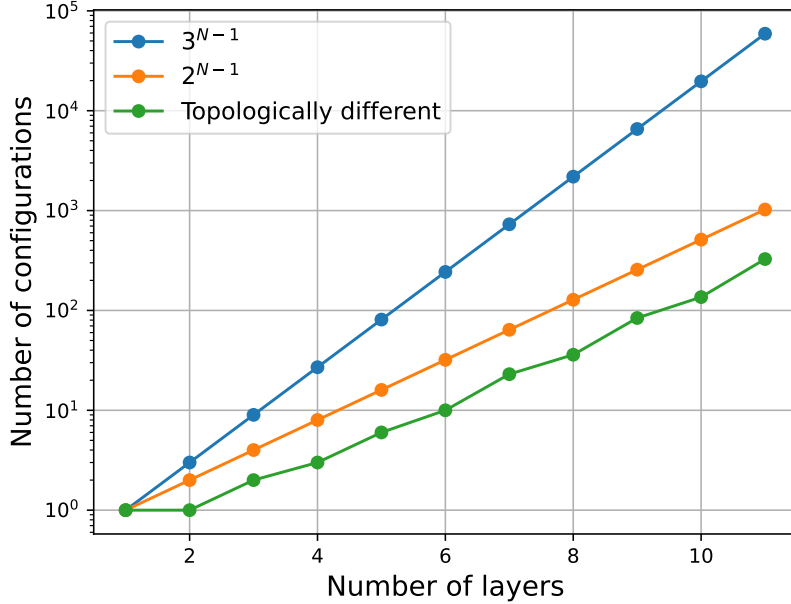


Figure 13: The number of configurations as the function of the number of layers. The blue line represents all configurations, even the ones that include AA stacking. The orange line excludes AA stacking. The green line has all the restrictions mentioned above.

We have successfully chosen only the necessary stacking orders in this section. In the next section, we will see how thicker systems have more atoms in their unit cell resulting in matrices of higher order, making it crucial to decrease the amount of calculations thus keeping the computational time manageable.

3.2 Tight binding model for stacking faults

The calculation of the band structure of bulk graphite has been performed by J. C. Slonczewski and P. R. Weiss in 1957 [55]. Their model is now widely known as the Slonczewski-Weiss-McClure (SWM) model. In the tight binding model we consider intra- and inter-layer hopping parameters γ_i between the p_z orbitals of neighbouring atoms. γ_0 is the intra-layer hopping introduced in section 2.3. We will introduce three inter-layer parameters between adjacent layers: γ_1, γ_2 and γ_3 . In addition we will also incorporate an on-site parameter δ . It is worth mentioning that hoppings between further neighbours could be taken into account as well [56], but it is outside of the scope of this thesis, therefore we will start with bilayer graphene and later see how the model is built from it.

3.2.1 The Hamiltonian of bilayer graphene

This part introduces the hoppings accounted for in our model through the example of a bilayer system. Following the reasoning of section:3.1 we will only look at AB stacking.

As we have seen in section:2.3, the tight binding model of graphene can be represented as a 2×2 matrix (see eq.:(34)). The reason for this is the two sublattice points in the unit cell. Subsequently each additional layer will contribute two more atoms, thus the matrix describing a sample of N layers will have the shape $2N \times 2N$. The Hamiltonian of a system with two layers can be written in general as:

$$\hat{H} = \begin{pmatrix} \hat{H}_{0_1} & \hat{H}_1 \\ \hat{H}_1^\dagger & \hat{H}_{0_2} \end{pmatrix}, \quad (55)$$

where \hat{H}_{0_i} is the intra-layer Hamiltonian, which in the case of bilayer graphene is the same in both layers making $\hat{H}_{0_1} = \hat{H}_{0_2} = \hat{H}_0$. The matrix \hat{H}_1 incorporates inter-layer interactions.

The one particle states in eq.:(20) get another degree of freedom L , indexing the layer they are in:

$|\alpha_L\rangle$. This way the state localized on the A sublattice of the first layer can be denoted as: $|A_1\rangle$.

Using this notation we can define the hopping integrals used in our model:

$$\begin{aligned} \gamma_0 &= \langle A_1 | \hat{H} | B_1 \rangle = \langle A_2 | \hat{H} | B_2 \rangle, \\ \gamma_1 &= \langle A_1 | \hat{H} | B_2 \rangle, \\ \gamma_2 &= \langle A_1 | \hat{H} | A_2 \rangle = \langle B_1 | \hat{H} | B_2 \rangle, \\ \gamma_3 &= \langle A_1 | \hat{H} | B_2 \rangle. \end{aligned} \quad (56)$$

To outline the \mathbf{k} -space Hamiltonian of the system, we require the phase factors corresponding to each hopping. The phase factor defined in section:2.3 can be rephrased as:

$$f(\mathbf{k}) = \sum_{R_n} e^{i\mathbf{k}\mathbf{R}_n}, \quad (57)$$

where R_n indexes the vectors pointing to the unit cells in which the atoms that take part in the corresponding hoppings reside. The observation can be made with the help of Fig.:14, that the appropriate neighbours are the following:

$$\begin{aligned} \mathbf{R}_{A_1 \rightarrow B_1} &= \mathbf{0}, -\mathbf{a}_1, -\mathbf{a}_2 \\ \mathbf{R}_{A_1 \rightarrow A_2} &= \mathbf{0}, -\mathbf{a}_1, -\mathbf{a}_2 \\ \mathbf{R}_{B_1 \rightarrow B_2} &= \mathbf{0}, -\mathbf{a}_1, -\mathbf{a}_2 \\ \mathbf{R}_{A_1 \rightarrow B_2} &= -(\mathbf{a}_1 + \mathbf{a}_2), -\mathbf{a}_1, -\mathbf{a}_2. \end{aligned} \quad (58)$$

3 RHOMBOHEDRAL GRAPHITE AND STACKING FAULTS

We should note here, that $\mathbf{R}_{B_1 \rightarrow A_2}$ does not have a phase factor because the sample is finite in the y direction. Applying this to eq.: (57) results in two different phase factors:

$$\begin{aligned} f(\mathbf{k}) &= 1 + e^{-i\mathbf{k}\mathbf{a}_1} + e^{-i\mathbf{k}\mathbf{a}_2} \\ \tilde{f}(\mathbf{k}) &= e^{-i\mathbf{k}(\mathbf{a}_1+\mathbf{a}_2)} + e^{-i\mathbf{k}\mathbf{a}_1} + e^{-i\mathbf{k}\mathbf{a}_2}. \end{aligned} \quad (59)$$

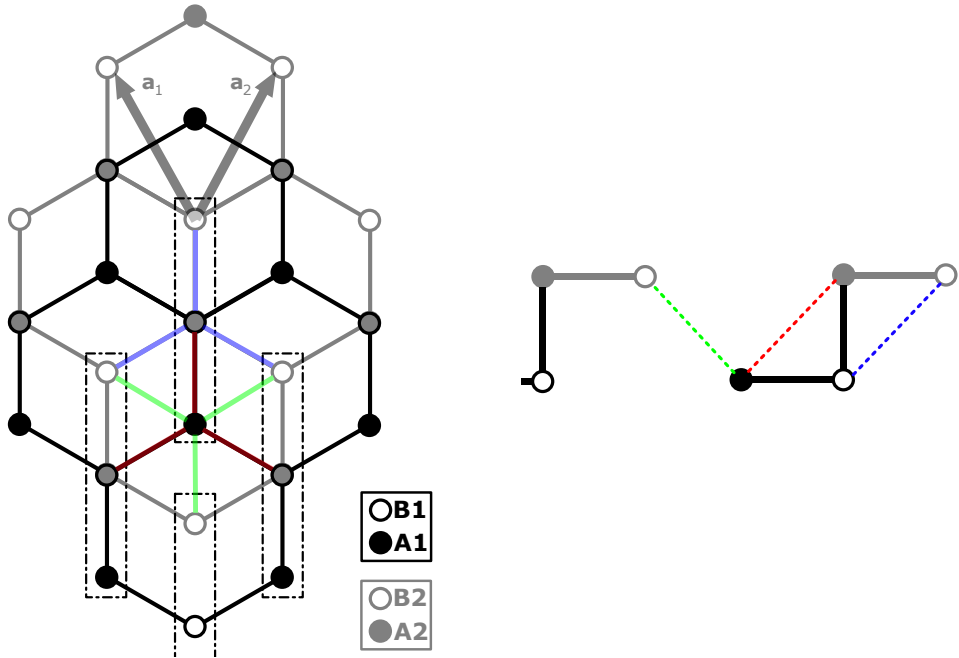


Figure 14: The lattice of AB stacked bilayer graphene. Each hopping is coloured. Black is the intra-layer hopping γ_0 , and on the right the vertical black line is the inter-layer interaction γ_1 between B_1 and A_2 . Red and Blue showcases the interactions between the same sublattices of the two layers with the amplitude γ_2 . Green indicates the hopping γ_3 , connecting A_1 to B_2 . This is the singular interaction that does not occur within the confines of the unit cell. The unit cells are encased with dashed line.

Utilizing the information gathered above we can express the momentum-space Hamiltonian in the shape:

$$\mathbf{H}(\mathbf{k}) = \begin{pmatrix} 0 & \gamma_0 f(\mathbf{k}) & \gamma_2 f(\mathbf{k}) & \gamma_3 \tilde{f}(\mathbf{k}) \\ \gamma_0 f^*(\mathbf{k}) & \delta & \gamma_1 & \gamma_2 f(\mathbf{k}) \\ \gamma_2 f^*(\mathbf{k}) & \gamma_1 & \delta & \gamma_0 f(\mathbf{k}) \\ \gamma_3 \tilde{f}^*(\mathbf{k}) & \gamma_2 f^*(\mathbf{k}) & \gamma_0 f^*(\mathbf{k}) & 0 \end{pmatrix}, \quad (60)$$

on the basis of $\Psi_{\mathbf{k}} \left(|A_1, \mathbf{k}\rangle, |B_1, \mathbf{k}\rangle, |A_2, \mathbf{k}\rangle, |B_2, \mathbf{k}\rangle \right)$. We should emphasize that here we already included the δ on-site parameter. This parameter is responsible for the asymmetry in the energy spectrum. (The inclusion of this parameter is detailed in section:3.2.2.) In Fig.:15 this difference can be observed. The Fourier transformation of the one particle state vectors is done the same way as in section:2.3.

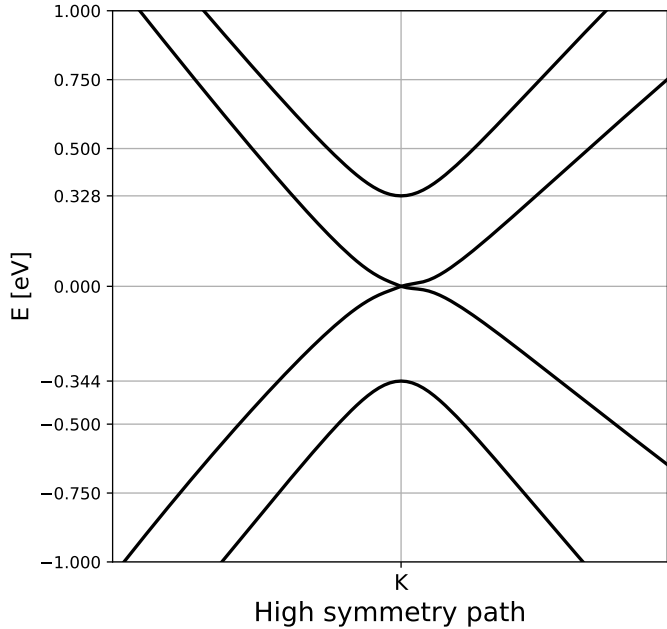


Figure 15: The band structure of bilayer graphene. An energy shift between the higher energy Valence and conduction bands can be noticed, which is due to the δ parameter.

The tight binding parameters were set to be consistent with Ref.:[57]. They can be seen in Table:1.

	δ	γ_0	γ_1	γ_2	γ_3
TB parameters [eV]	-0.0077	-2.59	-0.336	-0.146	-0.2655

Table 1: Tight binding parameters used in our model.

3.2.2 Few layer graphene and stacking faults

We have seen the function of inter-layer hoppings in the previous section. This part aims to build a model to describe a sample of few layer graphene (FLG) and how stacking faults appear in the Hamiltonian.

Eq.: (60) takes the form of the general bilayer tight binding model (eq.: (55)), where the submatrices belonging to the intra- and inter-layer hopping are the following:

$$\mathbf{H}_0(\mathbf{k}) = \begin{pmatrix} 0 & \gamma_0 f(\mathbf{k}) \\ \gamma_0 f^*(\mathbf{k}) & 0 \end{pmatrix}, \quad \mathbf{H}_1(\mathbf{k}) = \begin{pmatrix} \gamma_2 f(\mathbf{k}) & \gamma_3 \tilde{f}(\mathbf{k}) \\ \gamma_1 & \gamma_2 f(\mathbf{k}) \end{pmatrix}. \quad (61)$$

These matrices can be employed to derive a comprehensive expression that encompasses N layers of FLG in ABC order in the shape of a block diagonal matrix:

$$\mathbf{H}(\mathbf{k}) = \begin{pmatrix} \mathbf{H}_0(\mathbf{k}) & \mathbf{H}_1(\mathbf{k}) & 0 & \cdots & \cdots & 0 \\ \mathbf{H}_1^\dagger(\mathbf{k}) & \mathbf{H}_0(\mathbf{k}) & \mathbf{H}_1(\mathbf{k}) & \cdots & \cdots & 0 \\ 0 & \mathbf{H}_1^\dagger(\mathbf{k}) & \mathbf{H}_0(\mathbf{k}) & \mathbf{H}_1(\mathbf{k}) & \cdots & 0 \\ \vdots & & & \ddots & & \vdots \\ \vdots & & & & \ddots & \vdots \\ 0 & \cdots & \cdots & \cdots & \mathbf{H}_1^\dagger(\mathbf{k}) & \mathbf{H}_0(\mathbf{k}) \end{pmatrix}. \quad (62)$$

We can now address the issue of stacking faults. The intra-layer hopping matrix $\mathbf{H}_0(\mathbf{k})$ is not affected by stacking order. The difference resides in the inter-layer interaction $\mathbf{H}_1(\mathbf{k})$. A stacking fault can be defined in this work as a deviation from ABC stacking order as seen in Fig.:16. Due to the aforementioned constraints (section:3.1), this deviation can only mean that the next layer is displaced in the opposite direction as the layers below it.

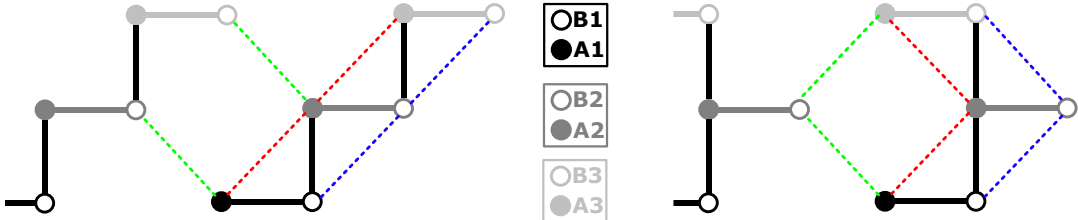


Figure 16: The hoppings accounted for in trilayer systems. The left hand side presents ABC stacking and displays the way the block diagonal matrix is built. The right hand side depicts ABA stacking, which can be understood as a stacking fault in the third layer.

Fig.:16 illustrates how the hoppings change in the case of a fault. Firstly, the vertical inter-layer interaction is realized between the A sublattice of the lower layer and the B of the upper one. The introduction of a stacking fault swaps the participating sublattices from A to B and vice versa. This sublattice change can also be observed in the case of the interaction indicated in green. All the inter-layer hoppings that also happen between different unit cells change direction. This affects

the phase factors associated to them while the neighbouring cells are in the opposite direction as described in eq.: (58). Substituting these vectors into eq.: (57) yields the complex conjugate of the original phases. The resulting inter-layer matrix is the adjoint of the original one:

$$\mathbf{H}_1^\dagger(\mathbf{k}) = \begin{pmatrix} \gamma_2 f^*(\mathbf{k}) & \gamma_1 \\ \gamma_3 \tilde{f}^*(\mathbf{k}) & \gamma_2 f^*(\mathbf{k}) \end{pmatrix}. \quad (63)$$

Thus the general method of building the matrix of FLG of thickness N is to change the inter-layer matrix to its adjoint in the appropriate positions. In the case of ABA the matrix would take the form:

$$\hat{\mathbf{H}}_{ABA} = \begin{pmatrix} \hat{H}_0 & \hat{H}_1 & 0 \\ \hat{H}_1^\dagger & \hat{H}_0 & \hat{H}_1^\dagger \\ 0 & \hat{H}_1 & \hat{H}_0 \end{pmatrix}, \quad (64)$$

The last parameter to take into account is the δ on-site energy introduced in eq.: (60). This parameter causes sublattice polarization and is applied to the model in the following way. Every atom that takes part in the hopping characterized by γ_1 gets one δ of on-site energy added for each adjacent atom in the y direction. In the case of ABC every atom obtains one δ except for the two ends:

$$\mathbf{H}_{ABC}(\mathbf{k}) = \begin{pmatrix} 0 & \gamma_0 f(\mathbf{k}) & \gamma_2 f(\mathbf{k}) & \gamma_3 \tilde{f}(\mathbf{k}) & 0 & 0 \\ \gamma_0 f^*(\mathbf{k}) & \delta & \gamma_1 & \gamma_2 f(\mathbf{k}) & 0 & 0 \\ \gamma_2 f^*(\mathbf{k}) & \gamma_1 & \delta & \gamma_0 f(\mathbf{k}) & \gamma_2 f(\mathbf{k}) & \gamma_3 \tilde{f}(\mathbf{k}) \\ \gamma_3 \tilde{f}^*(\mathbf{k}) & \gamma_2 f^*(\mathbf{k}) & \gamma_0 f^*(\mathbf{k}) & \delta & \gamma_1 & \gamma_2 f(\mathbf{k}) \\ 0 & 0 & \gamma_2 f^*(\mathbf{k}) & \gamma_1 & \delta & \gamma_0 f(\mathbf{k}) \\ 0 & 0 & \gamma_3 \tilde{f}^*(\mathbf{k}) & \gamma_2 f^*(\mathbf{k}) & \gamma_0 f^*(\mathbf{k}) & 0 \end{pmatrix}. \quad (65)$$

With ABA stacking the middle layer has an atom with two δ and the other one with zero:

$$\mathbf{H}_{ABA}(\mathbf{k}) = \begin{pmatrix} 0 & \gamma_0 f(\mathbf{k}) & \gamma_2 f(\mathbf{k}) & \gamma_3 \tilde{f}(\mathbf{k}) & 0 & 0 \\ \gamma_0 f^*(\mathbf{k}) & \delta & \gamma_1 & \gamma_2 f(\mathbf{k}) & 0 & 0 \\ \gamma_2 f^*(\mathbf{k}) & \gamma_1 & 2 \cdot \delta & \gamma_0 f(\mathbf{k}) & \gamma_2 f^*(\mathbf{k}) & \gamma_1 \\ \gamma_3 \tilde{f}^*(\mathbf{k}) & \gamma_2 f^*(\mathbf{k}) & \gamma_0 f^*(\mathbf{k}) & 0 & \gamma_3 \tilde{f}^*(\mathbf{k}) & \gamma_2 f^*(\mathbf{k}) \\ 0 & 0 & \gamma_2 f(\mathbf{k}) & \gamma_3 \tilde{f}(\mathbf{k}) & 0 & \gamma_0 f(\mathbf{k}) \\ 0 & 0 & \gamma_1 & \gamma_2 f(\mathbf{k}) & \gamma_0 f^*(\mathbf{k}) & \delta \end{pmatrix}. \quad (66)$$

This concludes the description of the model we used in this thesis. The subsequent section elaborates on the final requirement preceding the presentation of our findings, namely, the utilization of methods for the comparison of DOS spectra.

3.3 Comparison of DOS spectra

Now, that our model has been established it is necessary to compare the computed spectra. Our assumption is that similar configurations result in similar features in their DOS. To test this assumption we will first attempt to calculate cross-correlations. As we will see later the outcome of this is promising, but suboptimal. Due to this, we utilize a more intricate decision tree algorithm.

3.3.1 Cross-correlation of functions

Cross-correlation is a measure of similarity between two signals in the field of digital signal processing [58]. We could define an analytic measure of how correlated two functions $f(t)$ and $g(t)$ are, by the correlation function:

$$(g \star f)(\tau) = \int_{-\infty}^{\infty} g(t)f(t + \tau)dt, \quad (67)$$

where τ is the lag time (see Fig.:17). This lag time is meant to help identify the similarity in functions with their phase shifted. If two functions have similar time dependence there are τ values for which the integral:67 yields a high value for every t , thus they interfere constructively. The more similar two functions are the higher the value of the integral will be.

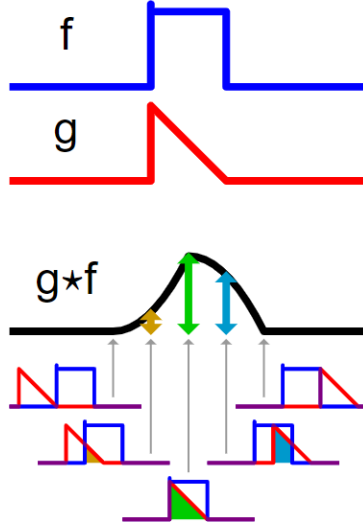


Figure 17: Cross-correlation of two functions f and g . The τ parameter is responsible for the sliding of function g . The cross-correlation is the area under the product of the f and g as the function of τ . Source:[59]

Our DOS spectra are not time-dependent of course. Nevertheless, all the aforementioned aspects can be reformulated in terms of energy by $t \rightarrow E$.

3.3.2 Decision tree model

Machine learning algorithms are on the rise nowadays. They can be utilized for a wide range of applications, from natural language processing and picture recognition to scientific research and medical diagnosis [60, 61, 62].

There is a huge variety of algorithms to choose from, each having their own advantages and disadvantages, thus it is not always trivial, which is the best to apply to a specific problem [63]. Machine learning models can be sorted into two main categories based on whether the data has labels or not. A label is essentially the value the algorithm should predict from the features of the data set. If no labels are available unsupervised learning algorithms are used to cluster the data by identifying underlying hidden patterns in it [64]. In our case the labels are known, since the DOS spectra are obtained from established configurations, therefore we need to employ a supervised learning algorithm. Within the set of supervised learning algorithms we can make a further division by the type of the labels. Regression models aim to predict a continuous value based on the given feature, while classification algorithms forecast the class of the data, i.e. a discrete value. As we only allow a discrete set of stacking orders and nothing in between, we should opt for classification. The model we ultimately settled on, is the decision tree classifier.

Decision trees are some of the most widely used machine learning algorithms. They can be utilized with non-linear problems because they do not rely on a linear classifier or regressor, but on a set of decisions. As a result, they are simpler to interpret relative to their counterparts. A decision tree, as the name suggests, can be thought of as a tree made of questions and decisions as shown in Fig.:18. On the very top of the tree there is the *root* or *root node*, the answer to this question leads to the *internal nodes* or *branches* of the tree. At the end of each branch there are other questions. A node with no further nodes attached is called a *leaf* or *leaf node* [65].

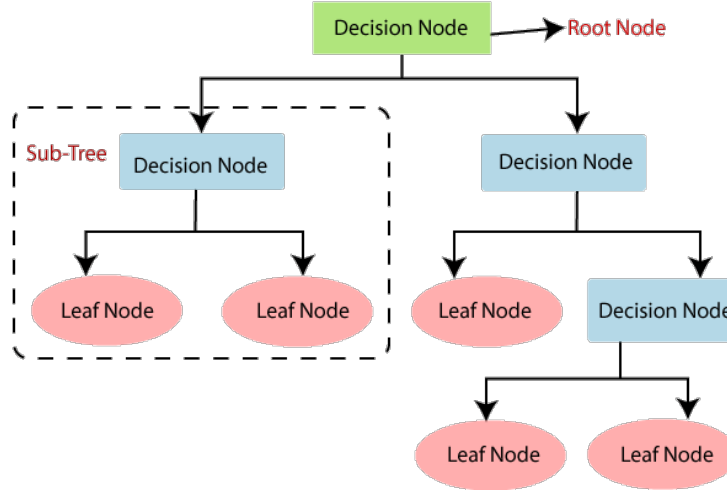


Figure 18: Simple picture of a decision tree. Source:[66]

To determine the order of the decisions we define the Gini impurity (named after Corrado Gini [67]). It quantifies the probability of misclassification for a randomly selected element when it is assigned a label. The minimum value is zero, which is given in the case when each node only contains elements from the same category. With N number of classes and p_n relative frequencies, i.e. the probability of choosing an element with label n in the data set, the Gini impurity is defined as:

$$I_G = 1 - \sum_n^N p_n^2. \quad (68)$$

Each individual node gets assigned a Gini impurity number. The node with the lowest number has leaves with the lowest impurity, hence it should be chosen as the root of the decision tree. To add more branches the same process can be repeated with the exclusion of the first node. Applying the final tree to an unknown element predicts a label for it.

This section have established the preliminaries important for the interpretation of our findings. In the following part we will look at the characteristics of PDOS spectra of the configurations detailed above. We will observe the difference between ABA and ABC stacking and how stacking faults can be identified.

4 Results

With all the preliminaries discussed in previous sections, we are prepared to analyze the findings of this thesis. Among others, one of the most important driving forces of this work was to aid in the identification of stacking faults from STM measurements. In this section we will see the most important characteristics of PDOS spectra. We will first look at the difference between ABA and ABC stacking. After studying the features of clean samples, we will examine the effect of thickness as well as the similarity between the spectra of a clean sample of fewer layers and a sample with stacking faults. Lastly, we will utilize numerical methods to outline the foundations of a tool that in the future could determine the stacking configurations from the measured STM spectra, helping the work of researches.

4.1 The fault-free systems

The easiest decision to make is whether a spectrum corresponds to the two limiting cases, ABA or ABC stacking. This is due to the peaks appearing in the low energy regime of ABC, but not in ABA, which resembles rather the *V* shape of simple graphene. This can be deducted from their band structure. From a perspective the DOS can be interpreted as the energy-wise distribution of states, thus a flat band at a given energy results in a peak in the spectrum. Fig.:19 showcases this phenomenon clearly. It depicts how the band structure translates to the PDOS. The flat band in the band structure of pure ABC creates a prominent zero energy peak in the PDOS. Looking at the spectra of each sublattice, it can even be observed that on the bottom layer the *A* atom (indicated in blue) and on the top layer the *B* atom (in orange) accommodates the peak. This means that low energy states localize at the edges of the system. This was expected, since there exists an analogy between rhombohedral graphite and the Su–Schrieffer–Heeger (SSH) model (introduced by Wu-Pei Su, John Robert Schrieffer and Alan Jay Heeger to describe polyacetylene [68]), which is a one-dimensional lattice, which in topological phase presents exponentially localized edge states of almost zero energy [69]. Smaller peaks can be found in the valance and conduction bands. We will refer to those as side bands. They indicate higher energy states occurring in the top and bottom layers. Another notable feature is the *drops* or *elbows* of the spectrum. They can be observed in both limiting cases and could be defined as steeper parts compared to the *V* baseline of graphene. They reside on the sublattice with a neighbour in the *y* direction for both ABA and ABC.

We should note that from here on we will only discuss the sum of the projected spectra of *A* and *B* atoms (indicated in green). The reason for this comes from the limitations of the measurements. There will be a contribution from neighbouring atoms, depending on the quality of the needle of

the STM and the ambient temperature.

$$\text{PDOS}_{\text{TOP/BOTTOM},\text{SUM}}(E) = \text{PDOS}_{\text{TOP/BOTTOM},A}(E) + \text{PDOS}_{\text{TOP/BOTTOM},B}(E). \quad (69)$$

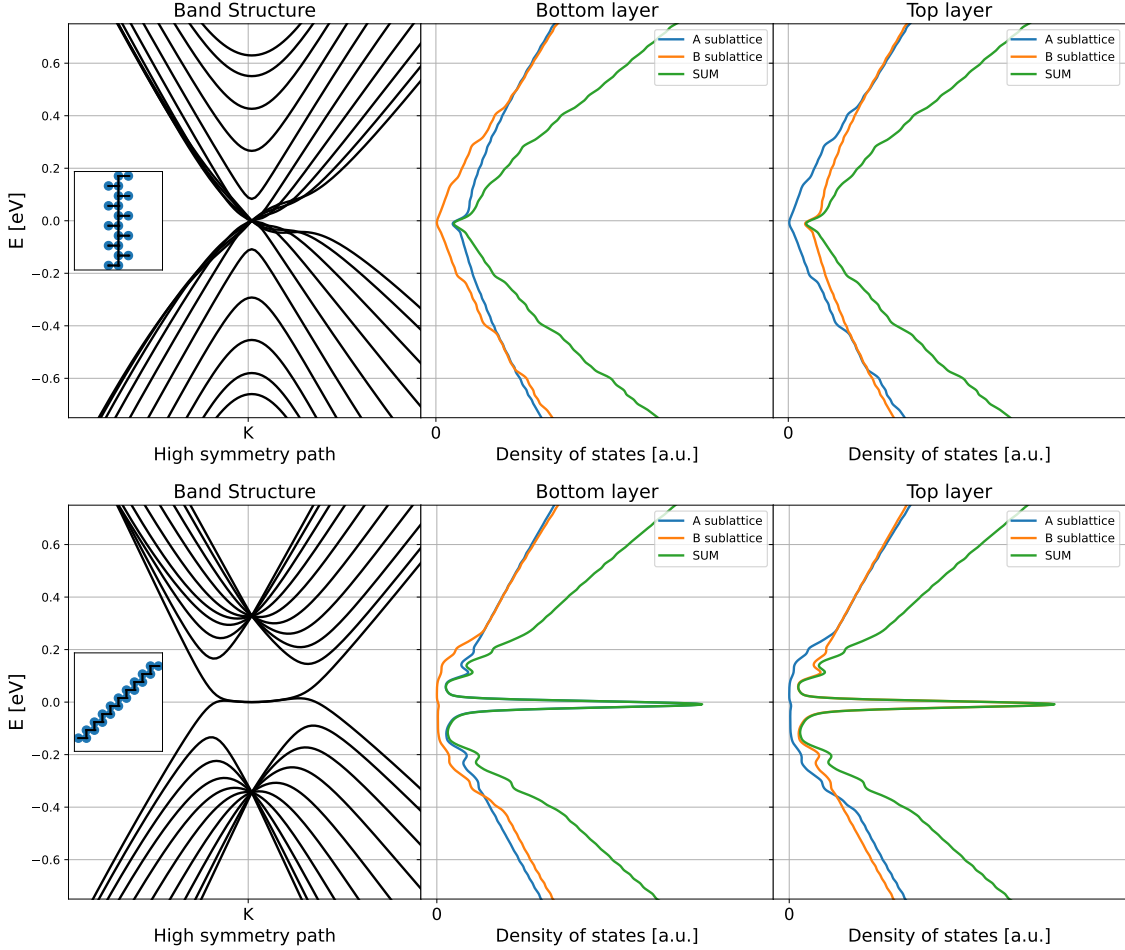


Figure 19: The left-most figures depict the band structure of ten layers of clean ABA (ABC) stacking on the top (bottom). The path taken in the Brillouin zone is $\Gamma \rightarrow \mathbf{K} \rightarrow \mathbf{M} \rightarrow \Gamma$. In the middle column the PDOS of the bottom layers can be seen. The right-most pictures display the spectrum of the top layers. It is worth noting, that because the symmetric structures the PDOS calculated are the same if we interchange the sublattices. They are indicated in blue and orange. The PDOS_{SUM} is coloured green.

4.2 The effect of thickness

Firstly, we will examine the changes in the PDOS spectrum of rhombohedral graphite as the number of layers increases as presented in Fig.:20.

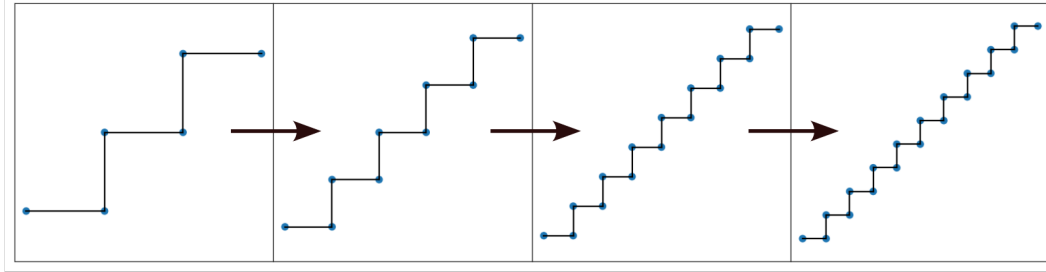


Figure 20: Increasing the number of layers. The blue dots indicate the atoms within the unit cell of each layer.

The best indicators of thickness are the energy of the peaks and the ratio between the peak heights of the side bands and the zero energy flat band. In Fig.:21a all PDOS spectra are plotted next to each other making the shift in energy of the side bands conspicuous. As we can observe in Fig.:21b the conduction side band moves more than 0.1 eV, while the valance side band gets closer to zero almost by 0.2 eV. With the growth of the thickness of the sample the zero energy peak gets more prominent compared to the side bands which is indicated by the increase of their ratio in Fig.:21c.

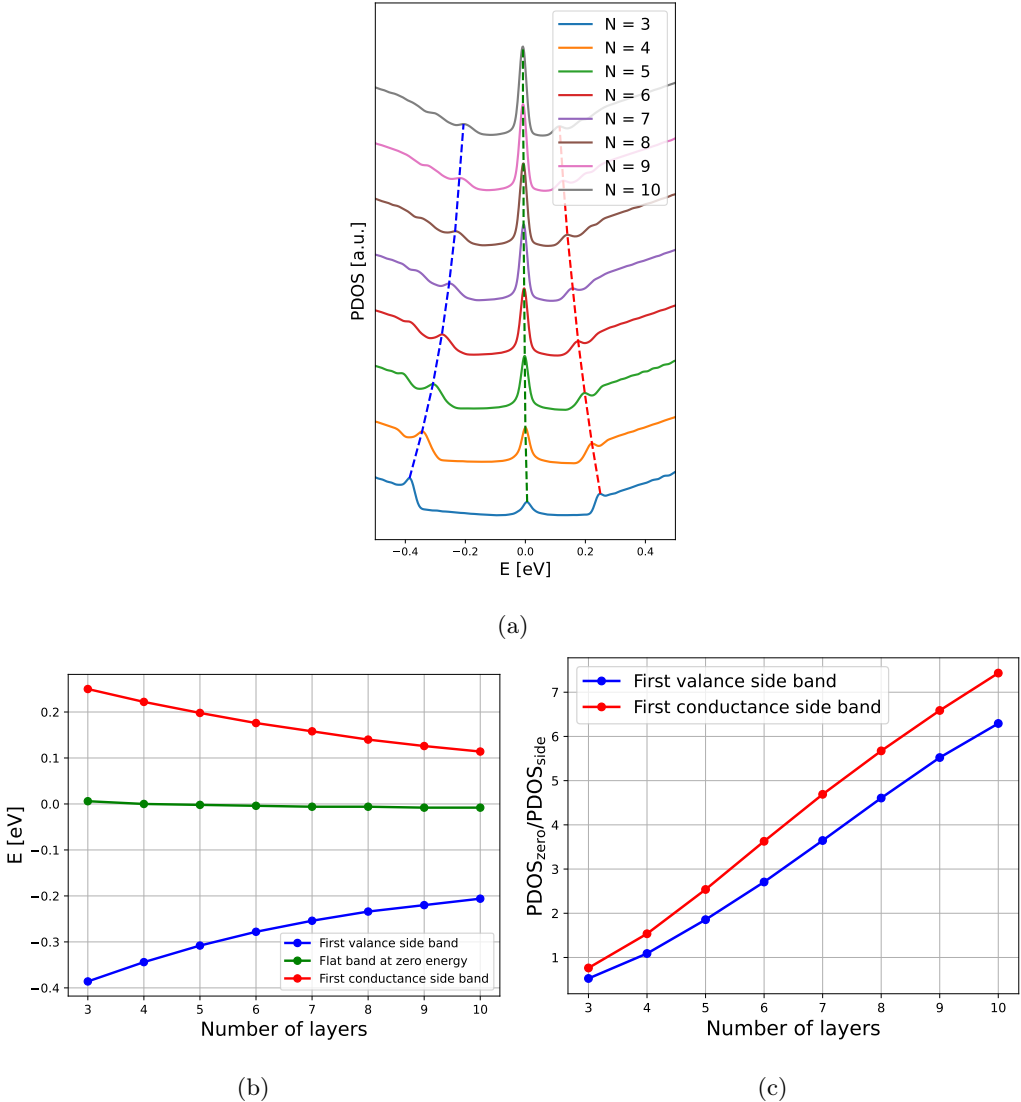


Figure 21: (a) depicts all PDOS spectra with the number of layers N growing towards the top of the figure. The dashed lines indicate the shift in the energy of the peaks. (b) shows this shift in detail. (c) illustrates the increase of the prominence of the zero energy peak compared to the side bands using their ratio.

4.3 The effect of a single fault

In this part we will take $N = 10$ layers of clean ABC graphite and introduce a stacking fault, then examine how the spectra of the top layer is altered with the depth of the fault.

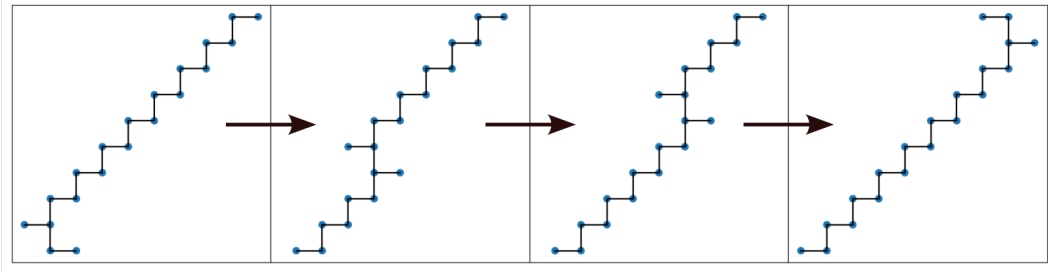


Figure 22: Moving the stacking fault from the second layer to the ninth.

Our assumption is that the spectrum resulting from a single stacking fault at depth d will resemble the spectrum of the clean system of thickness $N = d$. Studying Fig.:23 we can see this proven. In Fig.:23a the PDOS of the top layers are depicted next to each other. The first spectrum is ten clean layers then going upwards the stacking fault gets introduced closer and closer to the surface in the fashion portrayed in Fig.:22. The energy shift of the side bands can be observed in Fig.:23b, which demonstrates a clear link between the shifts of the clean samples as the number of layers grows and the shifts as the function of layers above the stacking fault. It is noteworthy that if the fault resides sufficiently close to the top, the usual ABC peaks disappear and peaks that shine through from lower layers take their place. They have similar, but lower energies than the clean sample underneath. In Fig.:23c the ratio of the peaks behaves in similar fashion as in the case of N -dependence. There is a crucial difference in the spectra of a sample with N layers and one with 10 layers and a fault at $d = N$ depth. Namely the prominence of the zero energy peak. This difference is highlighted in Fig.:23d as the pairwise ratio of the appropriate spectra. As expected thicker samples harbor higher zero energy peaks.

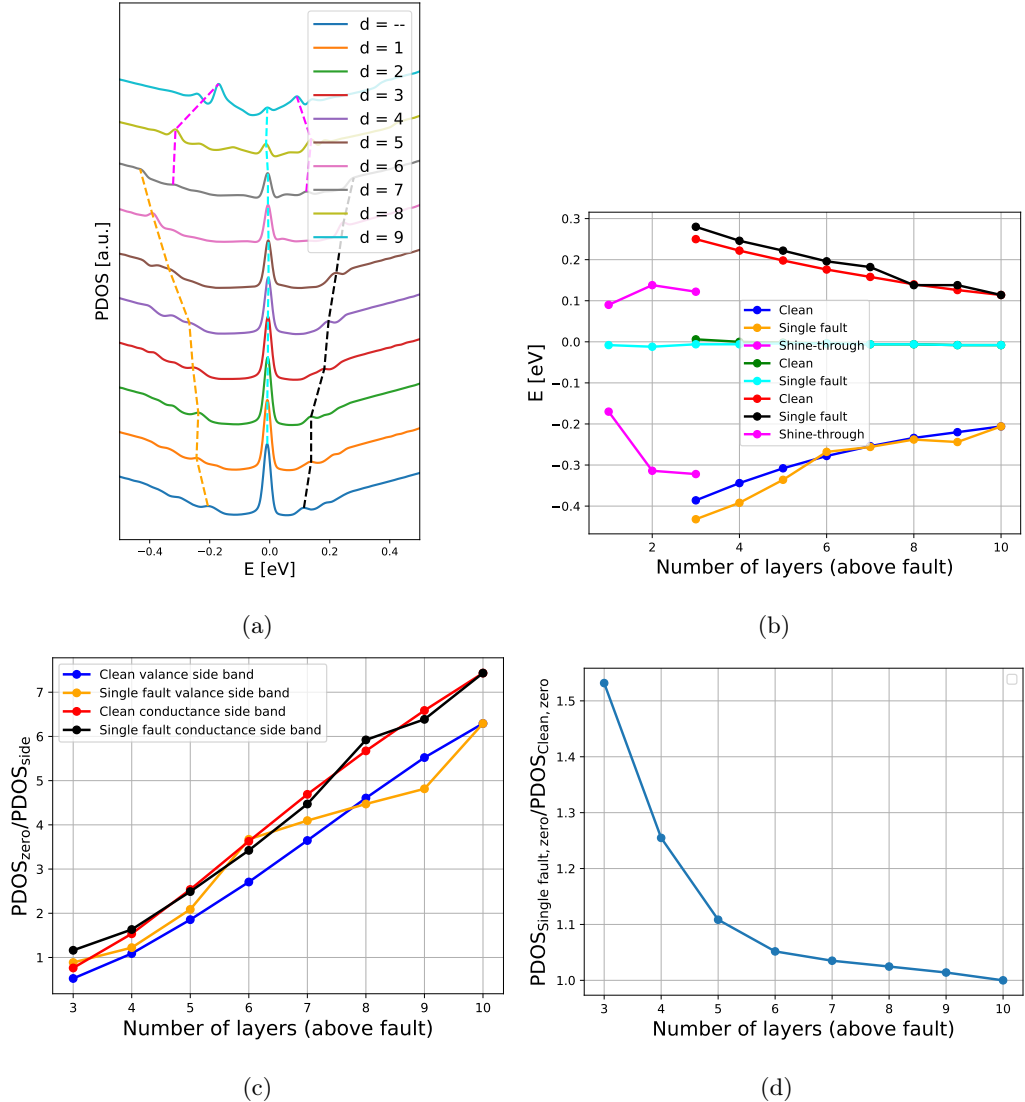


Figure 23: (a) shows all PDOS spectra with the stacking fault placed closer to the surface with each step upwards. The dashed lines indicate the shift in the energy of the peaks. (b) showcases this shift in detail, as well as the resemblance to the shifts of clean samples. (c) illustrates the increase of the prominence of the zero energy peak compared to the side bands using their ratio. (d) aims to depict the height difference of the zero energy peaks of the thinner clean samples and the ones with stacking faults introduced at the corresponding depth.

4.4 Transition from ABC to ABA

This section focuses on a similar alteration of $N = 10$ layers of ABC graphite as the previous one. The distinction is that instead of introducing a single stacking fault, we are transitioning the stacking order of the bottom portion of the system to ABA as illustrated in Fig.:24.

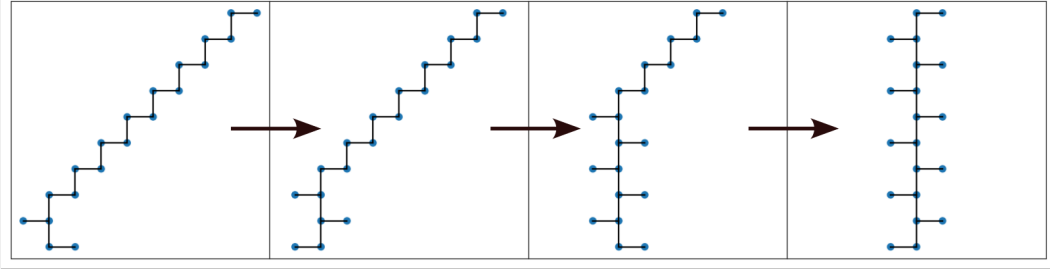


Figure 24: The transition from ABC to ABA.

Our assumption is the same as before. The spectra on the top layer should correspond to the number of clean ABC layers. This assumption once again proves to be valid. All PDOS spectra are plotted next to each other in Fig.:25a. The portion of ABA increases from the bottom to the top of the figure. As we can see the last spectrum has no visible peaks, which is expected as the system is entirely ABA, lacking ABC from underneath. Fig.:25b portrays the same energy shift can be observed mirroring the preceding two cases. The ratios of the side bands and zero energy peaks exhibit the same behaviour once again, which is evidently discernible in Fig.:25c. The height of the peaks at zero energy is almost the same as that of the corresponding clean systems, made apparent by Fig.:25d. This clearly distinguishes the spectra of these structures from the ones with a single stacking fault. From this result we can deduct that the height of the zero energy peak is influenced not only by the amount of ABC layers on top, but also by all of them in the configuration.

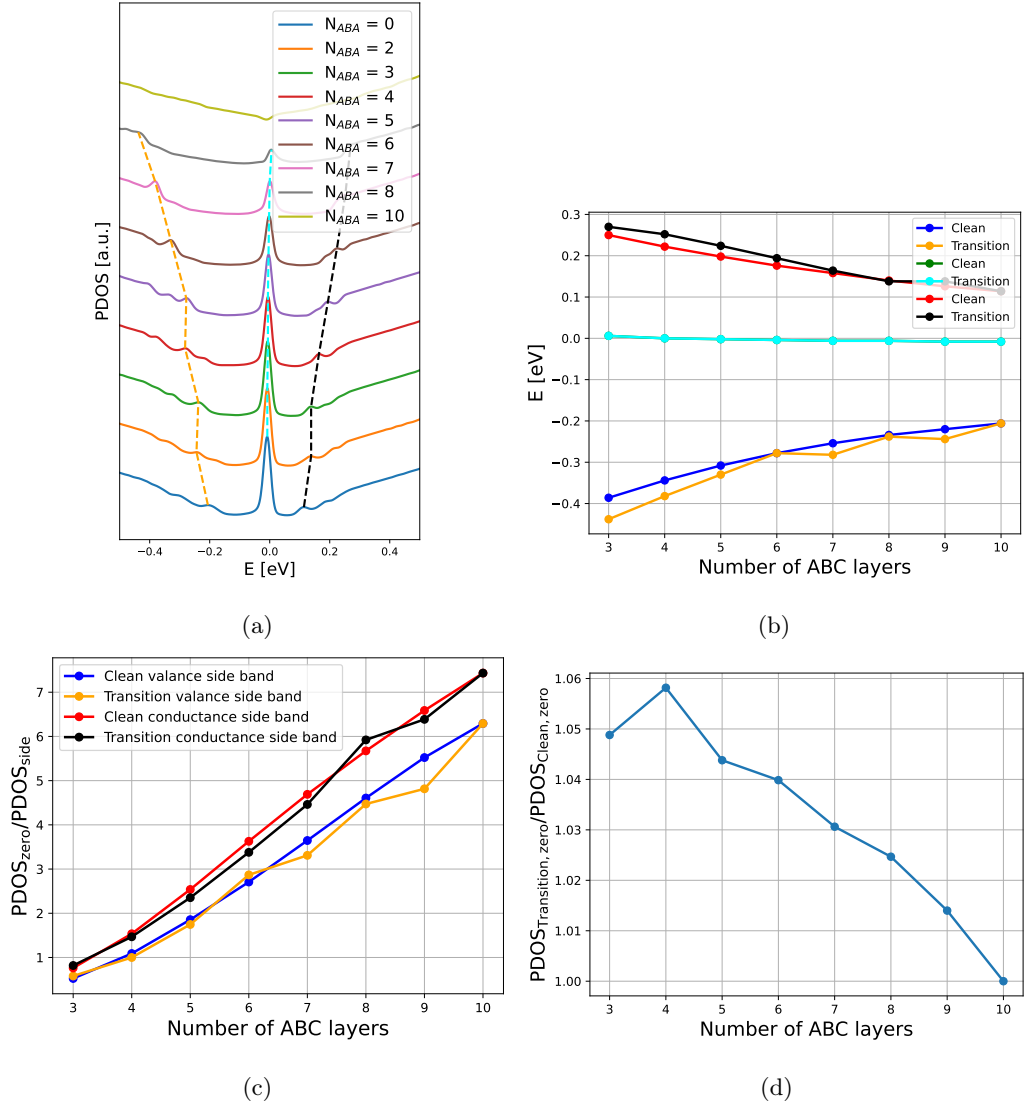


Figure 25: (a) displays all PDOS spectra with the ratio of ABA increasing towards the top of the figure. The dashed lines indicate the shift in the energy of the peaks. (b) expresses this shift in detail, as well as the resemblance to the shifts of clean samples. (c) demonstrates the increase of the prominence of the zero energy peak compared to the side bands using their ratio. (d) depicts the height difference of the zero energy peaks of the thinner clean samples and the ones with a transition from ABA and ABC. In this case the heights are almost the same, separating this case from the preceding one.

4.5 When do the peaks shine through?

In previous sections the question of ABC peaks shining through thin ABA structures came into our awareness. This part is dedicated to discover the details of this phenomena. The peaks of three ABC layers are still identifiable underneath seven layers of ABA. This is the most extreme case that we are capable of studying, since this is the thickest ABA structure and the thinnest ABC underneath that we have done the calculations for. As Fig.:27b shows, the energy shift is still observable, but not as clearly as before.

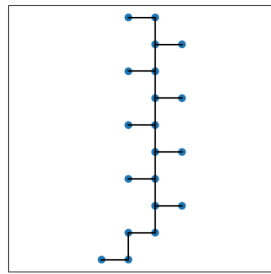


Figure 26: The most ABA layers that can still be shone through.

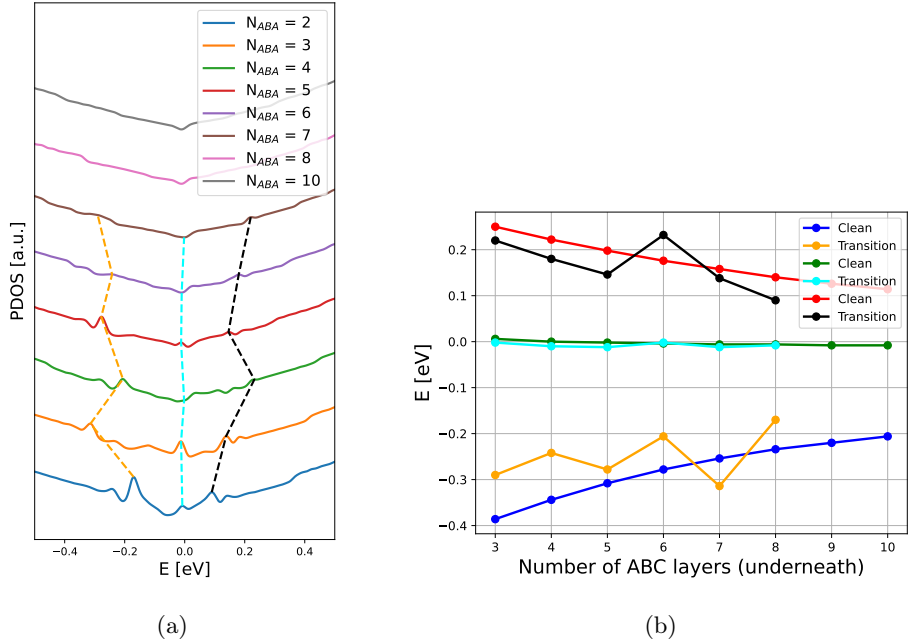


Figure 27: (a) portrays all PDOS spectra with the thickness of surface ABA increasing towards the top. (b) indicates the same trend of energy shift as before.

4.6 Algorithms to identify sub-structures

In prior sections, a number of promising features were explored that can aid in the endeavor to distinguish different structures based on their PDOS. The problem with this approach is when we start combining all manner of alterations to the structure, the number of possibilities increases greatly and the effect of one type of fault combines with the other, making it virtually impossible to identify the configurations by hand. The solution could be to utilize an algorithm to identify the traits of a spectrum in another one. The goal of such algorithm is to automatically identify a smaller sub-structure in a sample. This is the same task, what we did by hand previously. Just as we could pinpoint the characteristics of the spectrum of a few clean layers above a stacking fault or a transition to another type of stacking order, so should an appropriate algorithm be able to do the same and possibly even more.

4.6.1 Cross-correlation function

The cross-correlation of two functions is defined in section:3.3.1. In this part we will assume that the similarity of two spectra is directly proportional to their cross-correlation. As the energy of the peaks is a key factor we will take the value of the cross-correlation function at $\tau = 0$, so only peaks with similar energies interfere constructively. Since in section:4.5 we came to the conclusion that even seven layers can be shone through by the layers underneath, we will look at the correlations between all structures with $N \leq 9$ and those with $N = 10$ to try to identify the thickest possible sub-structures.

There are some promising results, but after the evaluation process we can declare that this approach is not adequate. The algorithm performs well on configurations with ABA on the surface as displayed in Fig.:28a. In contrast, ABC surfaces are almost always predicted to be $N = 9$ clean ABC, evident in Fig.:28b. This discrepancy originates from the immense area under the product of the zero energy peaks, which oppresses every other feature.

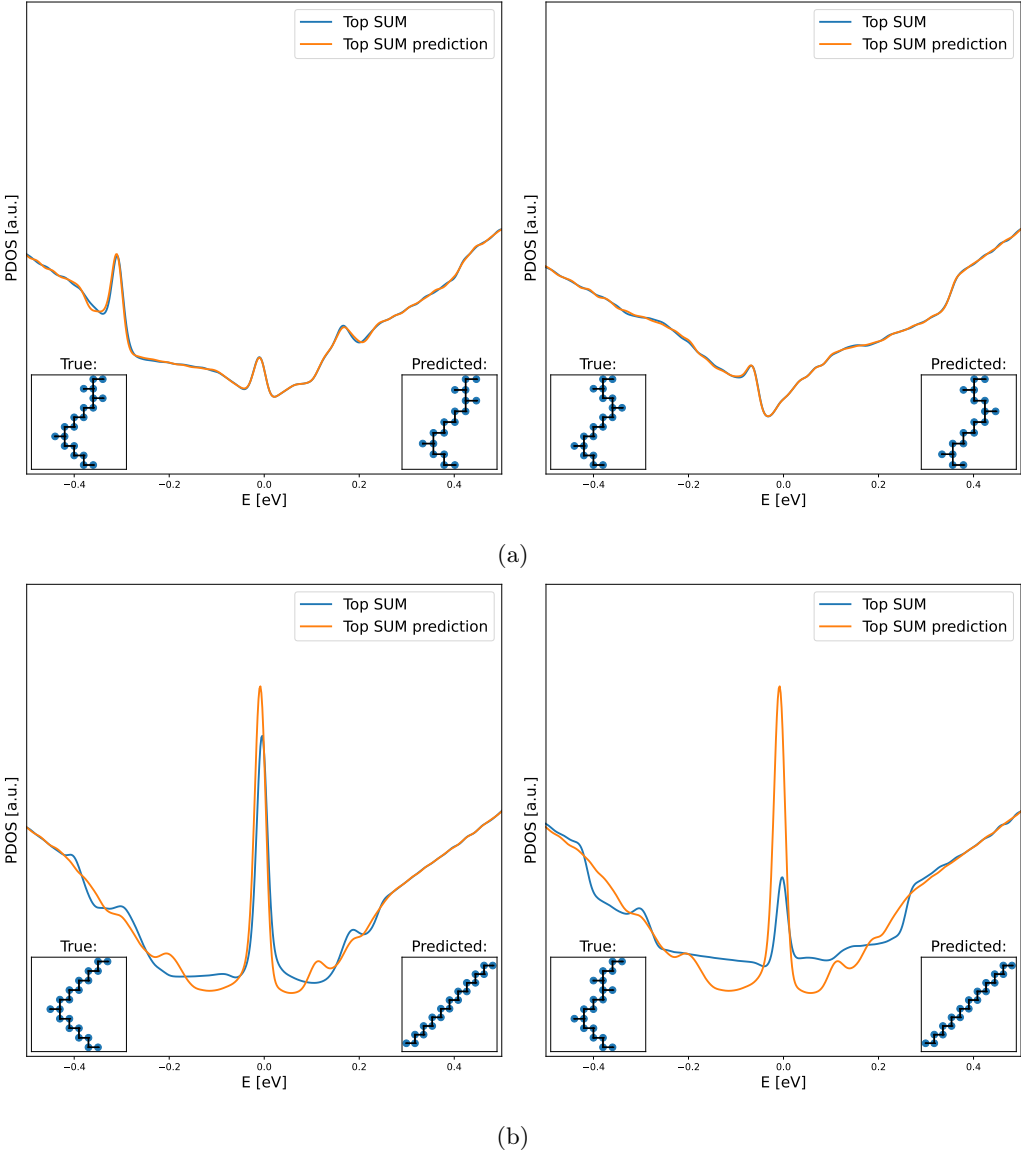


Figure 28: (a) displays predictions, which are correct to all nine layers. (b) brings two of the many examples, where the algorithm fails to perform.

4.7 The performance of the decision tree model

To overcome the limitations of the cross-correlation approach, we will utilize a decision tree model introduced in section 3.3.2. Machine learning algorithms require a training data set on which the model can be fitted. All configurations with $N \leq 9$ will be used for this purpose. Our test data set is all structures with $N = 10$ layers. The question we try to answer in this part is how many layers

can be correctly predicted from the surface PDOS. Firstly, we should see, that the shortcomings of the cross-correlation method indicated in Fig.:28b are resolved.

It is revealed in Fig.:29 that the decision tree model performs significantly better. Here we can also define how to count the number of matching layers. Based on the assumption, that there is a certain depth in which we can identify stacking order from just the surface of a sample, we count the number of layers from top that are in the same order in the prediction and in the real structure. The best case is when all nine layers of the prediction match. The worst result is two, which signifies that even the top was predicted incorrectly. Following this train of thought Fig.:29a earns a score of 9, while Fig.:29b achieves 8.

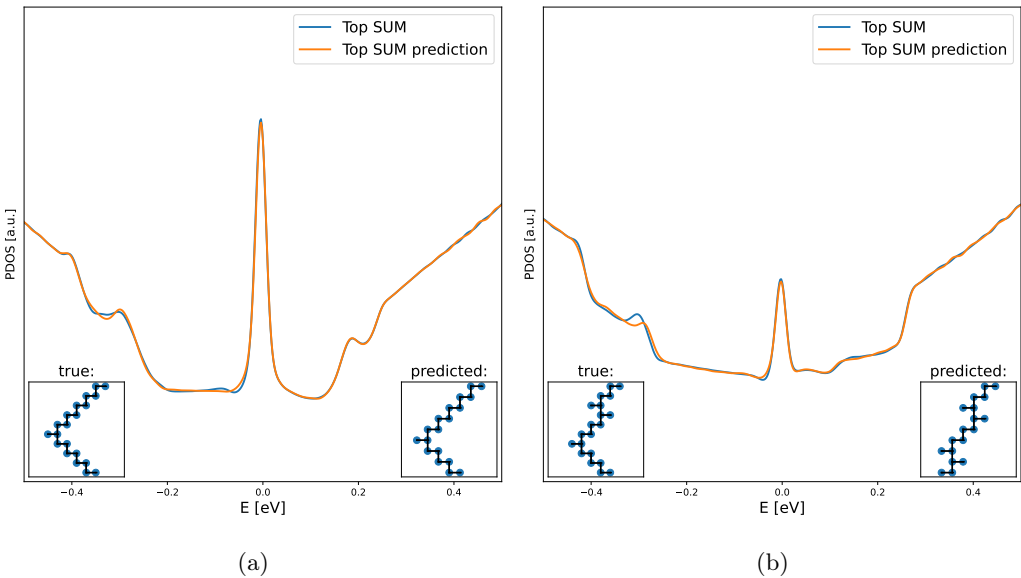


Figure 29: Predictions made by the tree model of configurations, that the cross-correlation failed.

Evaluating the entire test data set gives us insight on how many layers can be predicted correctly. Fig.:30 displays the distribution of the correctly predicted layers. Since the median is 8, we can state that in most cases the algorithm can be trusted to that depth.

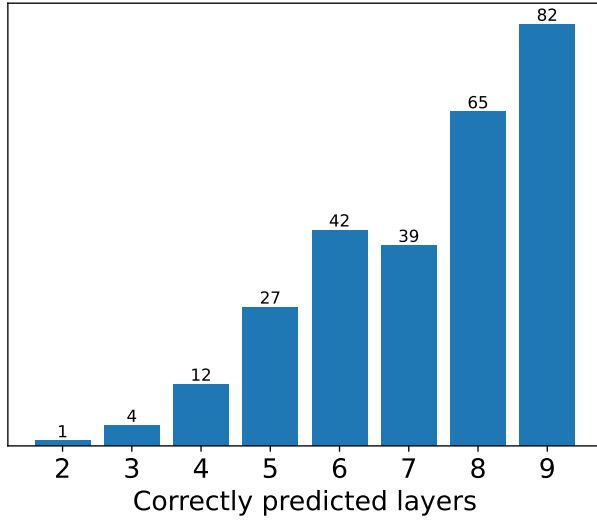


Figure 30: The evaluation of the entire test data set. Out of all 272 configurations predicted by the algorithm only one failed. The median of the correctly predicted layers is 8 and the expectation value is 7.3.

We have to address the issue of the single sample, that scored 2. This means that the model could not decide whether the structure on the top is ABA or ABC. The structure can be seen on Fig.:31. The algorithm compares the bottom PDOS of the true configuration to the top of the prediction. As we can see the real structure begins with three layers of ABC, but the prediction has ABA on top. The discrepancy could come from the shine-through peaks in the spectrum of the prediction.

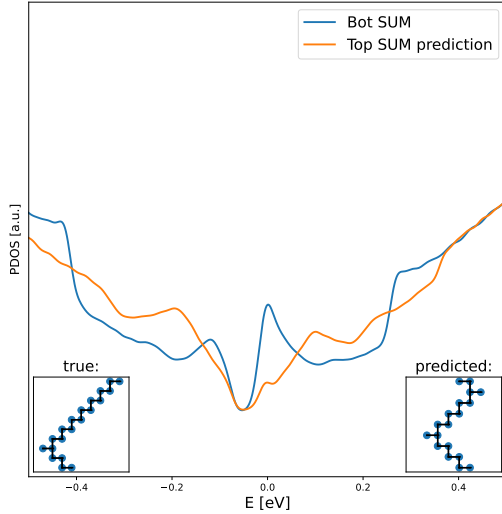


Figure 31: The only case, where the decision tree did not perform well.

5 Summary and outlook

In my thesis, I investigated the effects of stacking faults on the PDOS spectra of a rhombohedral graphite. Tight binding calculations were performed to obtain the spectra of all possible different configurations up to ten layers of few layer graphene. To reduce the vast number of computations and long time needed, only the topologically different ones were chosen. Notable effects of different alterations to the structures were studied in detail. It was clearly observed how the energy of the side bands gets closer to zero and compared to the peak at zero energy their prominence also diminishes as the number of layers increases. A clear correlation was discovered between the spectrum of a system with a single stacking fault introduced in a given depth and that of a clean sample with the corresponding thickness. This connection can also be noticed when transitioning the system from clean ABC to ABA order. While the effects of simple faults can be recognized, the convolution of the effects of more intricate sub-structures is challenging to describe. The comparison and differentiation was proved to be a highly complex task, not feasible by hand, thus the necessity for an algorithm arose. A decision tree was trained on the data set of samples with $N \leq 9$ and utilized to predict the structure of $N = 10$ samples, implying a depth to which such structures can be identified only by their surface PDOS. With the median of the depth of correct predictions being 8, we can state that in the majority of cases such an algorithm could be trusted to that extent.

This project sprouted from the initiative to aid in the identification of stacking order from STM measurements. The next step would be to test the model on STM measurement data from Péter Nemes-Incze's experimental group. In the future the tight binding model and the machine learning algorithm could be developed further, realising a tool that is beneficial for researchers.

References

- [1] Kannapan Panchamoorthy Gopinath, Dai-Viet N Vo, Dhakshinamoorthy Gnana Prakash, Antonysamy Adithya Joseph, Samynaathan Viswanathan, and Jayaseelan Arun. Environmental applications of carbon-based materials: a review. *Environmental Chemistry Letters*, 19:557–582, 2021.
- [2] Rajashree Hirlekar, Manohar Yamagar, Harshal Garse, Mohit Vij, and Vilasrao Kadam. Carbon nanotubes and its applications: a review. *Asian journal of pharmaceutical and clinical research*, 2(4):17–27, 2009.
- [3] Parand R Riley and Roger J Narayan. Recent advances in carbon nanomaterials for biomedical applications: A review. *Current Opinion in Biomedical Engineering*, 17:100262, 2021.
- [4] NobelPrize.org. <https://www.nobelprize.org/prizes/chemistry/1996/press-release/>.
- [5] NobelPrize.org. <https://www.nobelprize.org/prizes/physics/2010/summary/>.
- [6] N. D. Mermin and H. Wagner. Absence of ferromagnetism or antiferromagnetism in one- or two-dimensional isotropic heisenberg models. *Phys. Rev. Lett.*, 17:1133–1136, Nov 1966.
- [7] P. M. Chaikin and T. C. Lubensky. *Principles of Condensed Matter Physics*. Cambridge University Press, 1995.
- [8] Jannik C Meyer, Andre K Geim, Mikhail I Katsnelson, Konstantin S Novoselov, Tim J Booth, and Siegmar Roth. The structure of suspended graphene sheets. *Nature*, 446(7131):60–63, 2007.
- [9] Marina Filchakova. Multi-walled Carbon Nanotubes Production, Properties & Applications, 2021.
- [10] DDL Chung. Review graphite. *Journal of materials science*, 37(8):1475–1489, 2002.
- [11] Zhenhua Qiao, Shengyuan A Yang, Wanxiang Feng, Wang-Kong Tse, Jun Ding, Yugui Yao, Jian Wang, and Qian Niu. Quantum anomalous hall effect in graphene from rashba and exchange effects. *Physical Review B*, 82(16):161414, 2010.
- [12] Yuan Cao, Valla Fatemi, Shiang Fang, Kenji Watanabe, Takashi Taniguchi, Efthimios Kaxiras, and Pablo Jarillo-Herrero. Unconventional superconductivity in magic-angle graphene superlattices. *Nature*, 556(7699):43–50, 2018.

- [13] Paul Adrien Maurice Dirac. *The principles of quantum mechanics*. Number 27. Oxford university press, 1981.
- [14] Kostya S Novoselov, Andre K Geim, Sergei Vladimirovich Morozov, Da Jiang, Michail I Katsnelson, IVa Grigorieva, SVb Dubonos, Firsov, and AA. Two-dimensional gas of massless dirac fermions in graphene. *nature*, 438(7065):197–200, 2005.
- [15] Andre K Geim and Irina V Grigorieva. Van der waals heterostructures. *Nature*, 499(7459):419–425, 2013.
- [16] ML Ould Ne, M Boujnah, A Benyoussef, and A El Kenz. Electronic and electrical conductivity of ab and aa-stacked bilayer graphene with tunable layer separation. *Journal of Superconductivity and Novel Magnetism*, 30:1263–1267, 2017.
- [17] RR Haering. Band structure of rhombohedral graphite. *Canadian Journal of Physics*, 36(3):352–362, 1958.
- [18] John Desmond Bernal. The structure of graphite. *Proceedings of the Royal Society of London. Series A, Containing Papers of a Mathematical and Physical Character*, 106(740):749–773, 1924.
- [19] Chun Hung Lui, Zhiqiang Li, Kin Fai Mak, Emmanuele Cappelluti, and Tony F Heinz. Observation of an electrically tunable band gap in trilayer graphene. *Nature Physics*, 7(12):944–947, 2011.
- [20] Wenzhong Bao, Lei Jing, J Velasco Jr, Y Lee, Gang Liu, D Tran, B Standley, M Aykol, SB Cronin, D Smirnov, et al. Stacking-dependent band gap and quantum transport in trilayer graphene. *Nature Physics*, 7(12):948–952, 2011.
- [21] Imre Hagymási, Mohammad Syahid Mohd Isa, Zoltán Tajkov, Krisztián Márty, László Oroszlány, János Koltai, Assem Alassaf, Péter Kun, Konrád Kandrai, András Pálinkás, et al. Observation of competing, correlated ground states in the flat band of rhombohedral graphite. *Science Advances*, 8(35):eab06879, 2022.
- [22] M. Taut, K. Koepernik, and M. Richter. Electronic structure of stacking faults in hexagonal graphite. *Phys. Rev. B*, 88:205411, Nov 2013.
- [23] Auguste Bravais. Les systemes formes par des points distribués régulièrement sur un plan ou dans l'espace. *Journal de l'Ecole Polytechnique, XIX*, 1, 1850.

- [24] Jenö Sólyom. *Fundamentals of the Physics of Solids: Volume 1: Structure and Dynamics*, volume 1. Springer Science & Business Media, 2007.
- [25] L Brillouin. Les électrons libres dans les métaux et le rôle des reflexions de bragg. *J. phys. radium*, 1(11):377–400, 1930.
- [26] Wikipedia. Brillouin zone — Wikipedia, the free encyclopedia. <http://en.wikipedia.org/w/index.php?title=Brillouin%20zone&oldid=1154079679>, 2023. [Online; accessed 26-May-2023].
- [27] Erwin Schrödinger. An undulatory theory of the mechanics of atoms and molecules. *Physical review*, 28(6):1049, 1926.
- [28] Susumu Yamada, Toshiyuki Imamura, Takuma Kano, and Masahiko Machida. High-performance computing for exact numerical approaches to quantum many-body problems on the earth simulator. In *Proceedings of the 2006 ACM/IEEE Conference on Supercomputing*, pages 47–es, 2006.
- [29] Xiao Liang, Mingfan Li, Qian Xiao, Junshi Chen, Chao Yang, Hong An, and Lixin He. Deep learning representations for quantum many-body systems on heterogeneous hardware. *Machine Learning: Science and Technology*, 2023.
- [30] Max Born and W Heisenberg. Zur quantentheorie der moleküle. *Original Scientific Papers Wissenschaftliche Originalarbeiten*, pages 216–246, 1985.
- [31] Charles Augustin Coulomb. Premier mémoire sur l'électricité et le magnétisme. *Histoire de l'Académie Royale des Sciences*, 569, 1785.
- [32] Felix Bloch. Über die quantenmechanik der elektronen in kristallgittern. *Zeitschrift für physik*, 52(7-8):555–600, 1929.
- [33] J. C. Slater and G. F. Koster. Simplified lcao method for the periodic potential problem. *Phys. Rev.*, 94:1498–1524, Jun 1954.
- [34] Yaohua Tan, Michael Povolotskyi, Tillmann Kubis, Yu He, Zhengping Jiang, Gerhard Klimeck, and Timothy B Boykin. Empirical tight binding parameters for gaas and mgo with explicit basis through dft mapping. *Journal of Computational Electronics*, 12:56–60, 2013.
- [35] Zoltán Tajkov. Kétdimenziós hibrid nanorendszerök elméleti vizsgálata. Dec 2020.

- [36] Cserti József. Kétdimenziós kvantumrendszerök nanoszerkezetekben (two dimensional quantum systems in nanostructures). Master's thesis, (In Hungarian) MTA (Hungarian Academy of Sciences), MTA doktori dolgozat (DSc Thesis for Doctor of Science at Hungarian Academy of Sciences), 2009. MTA doktori dolgozat (DSc Thesis for Doctor of Science at Hungarian Academy of Sciences).
- [37] Daniel R Cooper, Benjamin D'Anjou, Nageswara Ghattamaneni, Benjamin Harack, Michael Hilke, Alexandre Horth, Norberto Majlis, Mathieu Massicotte, Leron Vandsburger, Eric Whiteway, et al. Experimental review of graphene. *International Scholarly Research Notices*, 2012, 2012.
- [38] Jiří Tuček, Piotr Błoński, Juri Ugolotti, Akshaya Kumar Swain, Toshiaki Enoki, and Radek Zbořil. Emerging chemical strategies for imprinting magnetism in graphene and related 2d materials for spintronic and biomedical applications. *Chemical Society Reviews*, 47(11):3899–3990, 2018.
- [39] Stephanie Reich, Janina Maultzsch, Christian Thomsen, and Pablo Ordejon. Tight-binding description of graphene. *Physical Review B*, 66(3):035412, 2002.
- [40] Jean Baptiste Joseph Fourier. *Théorie analytique de la chaleur*. Gauthier-Villars et fils, 1888.
- [41] Fritz Haake. *Quantum signatures of chaos*. Springer, 1991.
- [42] Brook Taylor. *Methodus incrementorum directa & inversa*. Inny, 1717.
- [43] Max Planck. *Über das gesetz der energieverteilung im normalspektrum*. Springer, 1978.
- [44] Gerd Binnig, Heinrich Rohrer, Ch Gerber, and Eddie Weibel. Tunneling through a controllable vacuum gap. *Applied Physics Letters*, 40(2):178–180, 1982.
- [45] Paul K Hansma, VB Elings, O Marti, and CE Bracker. Scanning tunneling microscopy and atomic force microscopy: application to biology and technology. *Science*, 242(4876):209–216, 1988.
- [46] Chunli Bai. *Scanning tunneling microscopy and its application*, volume 32. Springer Science & Business Media, 2000.
- [47] Gábor Mándi. Simulation of scanning tunneling microscopy from first principles. 2020.
- [48] Jerry Tersoff and Donald R Hamann. Theory of the scanning tunneling microscope. *Physical Review B*, 31(2):805, 1985.

- [49] J. Bardeen. Tunnelling from a many-particle point of view. *Phys. Rev. Lett.*, 6:57–59, Jan 1961.
- [50] Masato Aoki and Hiroshi Amawashi. Dependence of band structures on stacking and field in layered graphene. *Solid State Communications*, 142(3):123–127, April 2007.
- [51] Rui Xu, Long-Jing Yin, Jia-Bin Qiao, Ke-Ke Bai, Jia-Cai Nie, and Lin He. Direct probing of the stacking order and electronic spectrum of rhombohedral trilayer graphene with scanning tunneling microscopy. *Phys. Rev. B*, 91(3):035410, January 2015.
- [52] Changhua Bao, Wei Yao, Eryin Wang, Chaoyu Chen, José Avila, Maria C. Asensio, and Shuyun Zhou. Stacking-Dependent Electronic Structure of Trilayer Graphene Resolved by Nanospot Angle-Resolved Photoemission Spectroscopy. *Nano Lett.*, 17(3):1564–1568, March 2017.
- [53] N. B. Kopnin, M. Ijäs, A. Harju, and T. T. Heikkilä. High-temperature surface superconductivity in rhombohedral graphite. *Phys. Rev. B*, 87:140503, Apr 2013.
- [54] Rob H Telling, Chris P Ewels, Ahlam A El-Barbary, and Malcolm I Heggie. Wigner defects bridge the graphite gap. *Nature materials*, 2(5):333–337, 2003.
- [55] JC Slonczewski and PR Weiss. Band structure of graphite. *Physical review*, 109(2):272, 1958.
- [56] Edward McCann and Mikito Koshino. The electronic properties of bilayer graphene. *Reports on Progress in physics*, 76(5):056503, 2013.
- [57] Sergej Konschuh. Spin-orbit coupling effects: from graphene to graphite. 2011.
- [58] Rubin H Landau, Manuel J Páez, and Cristian C Bordeianu. *Computational physics: Problem solving with Python*. John Wiley & Sons, 2015.
- [59] Wikipedia. Cross-correlation — Wikipedia, the free encyclopedia. <http://en.wikipedia.org/w/index.php?title=Cross-correlation&oldid=1152157069>, 2023. [Online; accessed 19-May-2023].
- [60] Brady D Lund and Ting Wang. Chatting about chatgpt: how may ai and gpt impact academia and libraries? *Library Hi Tech News*, 40(3):26–29, 2023.
- [61] Sándor Kunsági-Máté, Róbert Beck, István Szapudi, and István Csabai. Photometric redshifts for quasars from wise-ps1-strm. *Monthly Notices of the Royal Astronomical Society*, 516(2):2662–2670, 2022.

- [62] Michał Kruczkowski, Anna Drabik-Kruczkowska, Anna Marciniak, Martyna Tarczewska, Monika Kosowska, and Małgorzata Szczerska. Predictions of cervical cancer identification by photonic method combined with machine learning. *Scientific Reports*, 12(1):3762, 2022.
- [63] Rishabh Choudhary and Hemant Kumar Gianey. Comprehensive review on supervised machine learning algorithms. In *2017 International Conference on Machine Learning and Data Science (MLDS)*, pages 37–43. IEEE, 2017.
- [64] Zoubin Ghahramani. Unsupervised learning. *Advanced Lectures on Machine Learning: ML Summer Schools 2003, Canberra, Australia, February 2-14, 2003, Tübingen, Germany, August 4-16, 2003, Revised Lectures*, pages 72–112, 2004.
- [65] James Thorn. Decision Trees Explained. <https://towardsdatascience.com/decision-trees-explained-3ec41632ceb6>, 2023. [Online; accessed 26-May-2023].
- [66] Java T point. Decision Tree Classification Algorithm. <https://www.javatpoint.com/machine-learning-decision-tree-classification-algorithm>, 2023. [Online; accessed 19-May-2023].
- [67] Corrado Gini. *Variabilità e mutabilità: contributo allo studio delle distribuzioni e delle relazioni statistiche.[Fasc. I.]*. Tipogr. di P. Cappini, 1912.
- [68] W. P. Su, J. R. Schrieffer, and A. J. Heeger. Solitons in polyacetylene. *Phys. Rev. Lett.*, 42:1698–1701, Jun 1979.
- [69] János K Asbóth, László Oroszlány, and András Pályi. A short course on topological insulators. *Lecture notes in physics*, 919:166, 2016.

Köszönetnyilvánítás

Szeretném megragadni az alkalmat, hogy köszönetet mondjak témavezetőimnek, Koltai Jánosnak és Tajkov Zoltánnak, akik nélkül ez a dolgozat nem készülhetett volna el. Köszönöm a támogatást, a jó tanácsokat, a motivációt, a lelkesítő szavakat és azt a rengeteg szakmai tudást, amit tőlük sajátíthattam el, nem csak ezzel a projekttel kapcsolatban, hanem végig az egyetemi tanulmányaim során. Szeretnék köszönetet mondani a türelmükért amikor a laptopommal ügyetlenkedtem, vagy egy huzamban egy hétag futott a kódomban. Hálás vagyok a biztatásukért is a PhD felvételi közben. Végül köszönettel tartozom Oroszlány Lászlónak is, aki ugyan most nem szerepelt témavezetőmként, de segítségért hozzá is bármikor fordulhattam.

2023.05.27.